

**This item is the archived peer-reviewed author-version of:**

Combined macroscopic, nanoscopic, and atomic-scale characterization of gold-ruthenium bimetallic catalysts for octanol oxidation

**Reference:**

Chinchilla Lidia E, Olmos Carol, Kurttepel Mert, Bals Sara, Van Tendeloo Gustaaf, Villa Alberto, Prati Laura, Blanco Ginesa, Calvino Jose J., Chen Xiaow ei, ....- Combined macroscopic, nanoscopic, and atomic-scale characterization of gold-ruthenium bimetallic catalysts for octanol oxidation  
Particle and particle systems characterization - ISSN 0934-0866 - 33:7(2016), p. 419-437  
Full text (Publisher's DOI): <https://doi.org/10.1002/PPSC.201600057>  
To cite this reference: <https://hdl.handle.net/10067/1349580151162165141>

## **Combined Macroscopic, Nanoscopic and Atomic-scale Characterization of Gold-Ruthenium Bimetallic Catalysts for Octanol Oxidation**

*Lidia E. Chinchilla<sup>1</sup>, Carol Olmos<sup>1</sup>, Mert Kurttepel<sup>2</sup>, Sara Bals<sup>2</sup>, Gustaaf Van Tendeloo<sup>2</sup>, Alberto Villa<sup>3</sup>, Laura Prati<sup>3</sup>, Ginesa Blanco<sup>1</sup>, José J. Calvino<sup>1</sup>, Xiaowei Chen<sup>1</sup>, Ana B. Hungría<sup>1\*</sup>*

<sup>1</sup> *Departamento de Ciencia de los Materiales, Ingeniería Metalúrgica y Química Inorgánica, Facultad de Ciencias, Universidad de Cádiz, Campus Río San Pedro, Puerto Real (Cádiz), C.P.11510, Spain*

<sup>2</sup> *Electron Microscopy for Materials Science (EMAT), University of Antwerp, Groenenborgerlaan 171, B-2020, Belgium*

<sup>3</sup> *Dipartimento di Chimica Inorganica Metallorganica e Analitica L.Malatesta, Università degli Studi di Milano, via Venezian 21, 20133 Milano, Italy*

E-mail: ana.hungria@uca.es

Keywords: Au-Ru bimetallics, ceria-zirconia, STEM-XEDS, octanol oxidation

A series of gold-ruthenium bimetallic catalysts of increasing Au:Ru molar ratios supported on a Ce<sub>0.62</sub>Zr<sub>0.38</sub>O<sub>2</sub> mixed oxide has been prepared and their structural and chemical features characterized by a combination of macroscopic and atomic scale techniques based on Scanning Transmission Electron Microscopy (STEM). The influence of the temperature of the final reduction treatment used as activation step (350 °C – 700 °C range) has also been investigated. The preparation method used allowed successfully preparing catalysts in which a major fraction of the metal nanoparticles is in the size range below 5 nm.

The structural complexities characteristic of this type of catalysts have been evidenced as well as the capabilities and limitations of both the macroscopic and microscopic techniques in the characterization of the system of metal nanoparticles. A positive influence of the addition of Ru on both the resistance against sintering and the catalytic performance of the starting supported Au catalyst is evidenced.

## 1. Introduction

The interest in catalytic materials based on gold arose decades ago by the discovery of the particular activity exhibited when this metal is in the form of small supported nanoparticles in a variety of reactions. We could cite, among others, hydrogenation of olefins<sup>[1]</sup>, hydrochlorination of ethyne to vinyl chloride,<sup>[2]</sup> low temperature CO oxidation,<sup>[3,4]</sup> or positional-selective oxidation of different alcohols.<sup>[5,6]</sup> It is well established in the literature that the activity of the supported gold catalysts is related to a high dispersion of the metallic particles.<sup>[6,7]</sup> The degree of dispersion of a catalyst can be determined by a multitude of parameters, including the method of preparation, the metal loading, the chemical nature of the metal precursor, the thermal pretreatment of the catalyst or the exact nature of the support.<sup>[4,8]</sup> One of the approaches described in the literature to increase the activity of gold systems is the addition of a second metal.<sup>[4,9-17]</sup> The synergy between the two metal phases could modify the active sites and improve the selectivity for certain products or promote the stability of the system.

To properly characterize this kind of complex systems, containing particles in the range of 1 to 10 nm, it is essential to provide an exhaustive analytical description at the nanometric scale, which correlates the particle size distribution with the nanoparticles composition. Typically, the determination of the particle size distributions and average particle size is performed by measuring a large number (100 – 200) of particles from electron microscopy images in TEM or STEM mode.<sup>[18-21]</sup> As for the composition, most studies present just a few XEDS analysis of individual nanoparticles to prove the presence of bimetallic particles (usually of varying composition) together with monometallic particles.<sup>[21-23]</sup> Only a few articles can be found in which a considerable effort is made to determine the composition of a large number of individual nanoparticles in order to obtain a statistically meaningful description of bimetallic catalysts and to establish a relationship between particle size and composition.<sup>[15,24,25]</sup> This kind of analysis, along with the information obtained from macroscopic techniques (ICP,

XRD and XPS) could facilitate the identification of the active species for a particular reaction, especially when compared to the reference monometallic catalysts.

This approach was used in a previous study in which we reported the characterization of Au and Ru bimetallic catalysts (with constant Au content and varying amounts of Ru) supported on a ceria-zirconia mixed oxide  $\text{Ce}_{0.62}\text{Zr}_{0.38}\text{O}_2$  by XRD, XPS and microscopy related techniques (HRTEM, HAADF-STEM, XEDS) as well as their performance for the selective oxidation of glycerol.<sup>[15]</sup> In the present work, we focus our attention on the liquid phase oxidation of octanol, representative of a long chain aliphatic alcohols,<sup>[26]</sup> using a similar bimetallic catalyst family in which, in contrast to our previous study,<sup>[15]</sup> the gold phase was stabilized against sintering by calcination at 250 °C before adding ruthenium. Macroscopic techniques (XRD, ICP, XPS and TPR) are complemented by HREM and HAADF-STEM studies measuring the size of at least 500 - 700 particles of each sample. In parallel, more than 75 particles across the size range were analyzed in each sample, in an attempt to identify the presence of bimetallic particles and to determine their composition range. The catalysts were submitted to several reduction treatments at increasing temperatures (350, 500, and 700 °C) to evaluate the effect of the presence of varying amounts of ruthenium on the stabilization of the systems against sintering.

## **2. Results and discussion**

The first major goal of this contribution was to establish the ultimate structural and compositional properties of the system of metal particles present in the synthesized Au-Ru catalysts on the basis of Transmission and Scanning Transmission Electron Microscopy techniques. This structural and compositional picture was analyzed in the framework of values of average properties determined by macroscopic techniques. From coincidences and deviations observed between approaches at these two scales, the possibilities and difficulties inherent to the local analysis techniques can be evidenced. Finally, data obtained in this in-

depth characterization study could provide the keys to understand changes in the catalytic performance in the process of interest, oxidation in the liquid phase of octanol. Therefore, in the following work, the focus is first placed on structural properties; macroscopic and then microscopic. After reporting on the catalytic activity and selectivity of the whole series of bimetallic catalysts, the influence of the addition of Ru to supported gold catalysts and, more particularly of the Ru loading, can be ascertained by comparison with the corresponding monometallic reference catalysts. Finally, putting together functional and structural information, some proposals about the origin of the modifications of the catalytic performance can be advanced.

## **2.1. Characterization at the macroscopic scale**

### *2.1.1. Specific Surface Area and Average composition*

Table 1 gathers the values of Au and Ru contents as determined by ICP-AES. Data expressed in weight and molar percent of both the bimetallic and the monometallic reference catalysts, are included. The Table also provides information about molar loading of the two metals per gram of catalyst. Note that the total content of Ru atoms in the monometallic catalyst, RuCZ, is roughly double that of Au atoms in AuCZ. As described in the experimental section, during the preparation of the bimetallic catalysts, Ru was added by incipient wetness impregnation in a second step, in all cases on the same previously prepared AuCZ catalyst. Therefore, the total Au molar content remains constant for all the bimetallic catalysts. Increments in the Ru content appear as increasing Ru molar contents and, concomitantly, as increasing total number of moles of metallic atoms in the bimetallics. Two of the three bimetallic catalysts present a total metal molar content close to that of the monometallic RuCZ. Only in the bimetallic with the highest Ru percent, 1:2.4 AuRuCZ-R350, the total metal content becomes larger.

The values of the specific surface area of all the prepared catalysts remain very close to that of the starting  $\text{Ce}_{0.62}\text{Zr}_{0.38}\text{O}_2$  (CZ) support oxide,  $20 \text{ m}^2\text{g}^{-1}$ . The differences between them fall within the experimental error, this indicating that the incorporation of the metal components did not significantly modify the surface texture of the initial ceria-zirconia oxide.

As detailed in the experimental section, the starting AuCZ catalyst was activated by calcination at  $250 \text{ }^\circ\text{C}$  after the incorporation of the gold precursor by the Deposition-Precipitation method (DP). Likewise, after the addition of the Ru precursor to this AuCZ catalyst by incipient wetness impregnation, a second activation treatment was used to transform the ruthenium precursor into the metallic component. In this case a reduction treatment at moderate temperature,  $350 \text{ }^\circ\text{C}$ , was used instead, since it is well established that the use of oxidation treatments with Ru precursors usually leads to very large particles.<sup>[27]</sup>

A Temperature Programmed Reduction ( $\text{H}_2$ -TPR) experiment was carried out in order to confirm that this pretreatment was adequate to guarantee the total transformation of the Ru precursor. The results obtained on the 1:1.3AuRuCZ catalyst have been included in **Figure S1** of Supporting Information. In particular, data of mass/charge (m/q) ratios of 2 and 18, corresponding to consumption of  $\text{H}_2$  and the evolution of water during the reduction process, are plotted in Figure S1(a) and S1(b) respectively. Note first that hydrogen consumption correlates perfectly with the evolution of water, showing two distinct peaks at roughly  $100$  and  $123^\circ\text{C}$ . Moreover, the decomposition of the precursor takes place mostly within the  $100$ - $200 \text{ }^\circ\text{C}$  temperature range. The first, narrow, peak can be attributed to the reduction of the Ru precursor, since Au was already in reduced state, whereas the second results from the reduction of the ceria-zirconia support.  $\text{H}_2$ -TPR results corresponding to m/q ratios of 15, 16

and 17, which provide additional information about the reduction of nitrates in the precursor, indicate that at least 350 °C are necessary to guarantee complete removal of these species.

A comparison of the H<sub>2</sub>-TPR results of the bimetallic catalyst with those of RuCZ, AuCZ and the bare CZ support, Figure S1(c) and **Figure S2 (b)**, provides interesting information. Note first how the reduction effects in the bimetallic catalyst take place at lower temperatures than in the monometallic ones; 100 °C-123°C in the former vs 180 °C in RuCZ or 140 °C in AuCZ. This points out that the presence of gold in the catalyst allows reducing the Ru precursors at much lower temperatures. Likewise, it also indicates that the reduction of the support is also facilitated in the presence of both metals. This can be related to the previously established ability of Au nanoparticles to dissociate and activate the H<sub>2</sub> molecule during adsorption.<sup>[28]</sup> This activated hydrogen would facilitate the reduction of the ruthenium precursors. Once both metals are reduced, the higher extent of the metal||support interface would make faster the reduction of the support itself. Also note the comparison of the H<sub>2</sub>-TPR traces of both monometallic catalysts with that of the bare support clearly points out to a largely enhanced reducibility of the ceria-zirconia oxide in the presence of any of the two supported metals.

These H<sub>2</sub>-TPR results indicate that 350 °C is an adequate temperature to guarantee the transformation of the precursors to their metallic state and also point out an interaction between the two supported metals and of the metals with the oxide support.

### *2.1.2. X-Ray Diffraction*

**Figure 1**, **Figure 2** and **Figure 3** show the XRD diagrams recorded on 1:0.7AuRuCZ, 1:1.3AuRuCZ, and 1:2.4AuRuCZ respectively, after reduction at the three assayed activation temperatures, 350 °C, 500 °C and 700 °C. XRD corresponding to the monometallic references

Au and Ru after reduction at increasing temperatures are included as supporting information in **Figure S3** and **Figure S4**.

Concerning the support, XRD diagrams contain the diffraction peaks expected for a ceria-zirconia oxidized pyrochlore, independently of metal loading or reduction temperature. Thus the most intense peaks observed at 29.15°, 33.75°, 48.55° and 57.45 ° correspond to the (222), (400), (440), and (622) planes of this phase. Therefore, neither the incorporation of the metallic components nor the reduction treatments induce structural transformations in the support oxide. It is important to stress that before the deposition of the metals, the support was previously treated under hydrogen at 950 °C and further oxidized at 600 °C. Further details about the structural transformations of the support used in this study after different redox treatments can be found elsewhere.<sup>[29,30]</sup>

**Figure S5** shows simulations that allow understanding the XRD results related to the metallic phases. In particular, diagrams calculated for a catalyst made up by a 98% wt. pyrochlore type  $\text{Ce}_{0.62}\text{Zr}_{0.38}\text{O}_2$  oxide, 1% wt. Au and 1% wt. Ru are presented. One of the diagrams, **Figure S5(a)**, considers metal nanoparticles 20 nm in diameter, whereas the second, **Figure S5(b)**, was calculated for 5 nm particles.

Note that the most intense, (111) Au peak lies close to the (100) Ru peak. Nevertheless, despite the total number of Ru atoms in the calculation is roughly double that of Au atoms, the Ru signal is much lower than that of Au. This is due to the large differences in the structure factors of the two reflections ( $F_{(111)} \text{Au} = 27.02 \text{ \AA}$ ,  $F_{(100)} \text{Ru} = 5.10 \text{ \AA}$ ) and in their multiplicities. Therefore, the peak at 38° provides information both on Au and Ru nanoparticles but with a major contribution from the former. In the case of the peaks at about 44°, corresponding to Ru (101) and Au (200), the contribution of the two metals is roughly the

same.  $F_{(200)} \text{ Au} = 24.05 \text{ \AA}$  is higher than  $F_{(101)} \text{ Ru} = 7.92 \text{ \AA}$  but the multiplicity of the second reflection is much higher and the number of Ru atoms is also much higher, this resulting in this case in diffraction peaks of roughly the same intensity. Finally when the particle size decreases down to 5 nm, all the diffraction peaks become very broad with very small intensities at their maxima.

Focusing on the metallic components, the diagrams of the monometallic catalysts, Figures S3 and S4, do not show signals characteristic of either Au or Ru, except for the AuCZ catalyst after reduction at the highest temperature, 700 °C. In this case a very broad and weak diffraction feature is observed at about 38°, indicating the occurrence of Au sintering. This effect is not observed in the case of the pure RuCZ catalyst, in which the signal in the 38°- 48°  $2\theta$  range remains at the noise level.

Likewise, the whole set of diagrams recorded on the bimetallic catalysts show in general very weak and broad signals at the positions (38°- 48°  $2\theta$  range) characteristic of either Au or Ru; this indicating that the metallic particles present in these catalysts are in general well dispersed, in the form of nanometer sized objects.

In the XRD diagrams of the 1:0.7 AuRuCZ-R350 and 1:0.7 AuRuCZ-R500 catalyst, Au or Ru peaks are not observed and only a quite subtle signal of (111) Au is observed in the catalyst reduced at the highest temperature, 1:0.7 AuRuCZ-R700. The signal at the position of the most intense Ru diffraction peaks characteristic of hcp Ru (i.e. 44.1°) remains at the noise level, even after reduction at 700 °C. This indicates that the metal particles in this catalyst remain mostly under the 5 nm size range; that the Ru metal particles are smaller than the Au particles, and that only moderate Au sintering is occurring at the highest temperature. No signs of intermetallic or alloy type particles could be found in the XRD diagrams.

In the catalyst with medium Ru content, 1:1.3 AuRuCZ, the results are very similar. Now the (101) Ru peak signal at 44.1° is better resolved, especially after reduction at 500 °C and 700 °C, possibly due to the higher Ru content. In parallel, the diffraction feature at 38.1° is also better observed. This peak contains contributions from both Au (111) and Ru (100), though the width of the peak is quite close to that in the 1:0.7 AuRuCZ-R700 catalyst. The higher Ru content in this catalyst is possibly contributing to this effect, but growth of gold cannot be disregarded. Although a more quantitative assessment of the average particle size is performed in a further section, these diagrams suggest that there is not a large difference in the average size of the metal nanoparticles between this catalyst and the previous one, and that most of the particles remain with size below 5 nm, especially after reduction at 350 °C and 500 °C.

Au and Ru diffraction peaks are best observed in the diagrams corresponding to the catalyst with the highest Ru content, 1:2.4. The signal at 44.1°, due to the Au (200) and Ru (101) peaks is not identified after reduction at 350 °C, but it clearly appears in the other two diagrams, 1:2.4 AuRuCZ-R500 and 1:2.4 AuRuCZ-R700. In the latter, this peak is clearly observed which suggests that a fraction of Au and Ru rich particles larger than 5 nm are present. The growth of the peak at 38° agrees also with a higher contribution from large Au or Ru particles. Peaks are still rather broad in all cases, this suggesting that a large fraction of the nanoparticles is still below 5 nm, especially in the catalyst reduced at 350 °C. As shown later, a combined STEM-HAADF and STEM-XEDS study is necessary to reveal the exact influence of reduction temperature and catalyst composition on the growth of the different types of particles present in these catalysts.

### 2.1.3 X-Ray Photoelectron Spectroscopy (XPS)

Tables 2 and 3 provide binding energy values of gold and ruthenium phases on the mono- and bimetallic catalysts as determined by XPS measurements. As an illustration, when 1:2.4 AuRuCZ-R350 catalyst is studied, the Au 4f 7/2 signal contains only one peak at 84.3 eV, which is assigned to metallic Au<sup>0</sup> in the form of small particles.<sup>[31,32]</sup> The shift of the Au 4f7/2 core-level peak to higher energies, relative to the bulk value of 84.0 eV, has been attributed to a particle size effect.<sup>[33]</sup> This value of binding energy is also smaller than that observed in other gold catalysts supported on ceria-zirconia prepared in our lab, which showed dispersion values in the order of 50%.<sup>[28]</sup> Such a result therefore suggests that the dispersion of Au in this bimetallic catalyst should be smaller than 50%.

In the case of Ru, both the 3d5/2 and 3p3/2 peaks show two different contributions, one at a low energy (281.8 and 463.9 eV and respectively) and a second one at a higher binding energy (283.1 and 474.6 eV respectively). The analysis of the 3d5/2 signal requires the precise deconvolution of the overlapping C 1s contribution. According to literature, the component at lower binding energies could be assigned to Ru in metallic state in the form of small particles, due to the shift with respect to reference values for bulk Ru (279.7-280.2 eV for Ru 3d5/2 and 461.1-462.2 eV for Ru 3p3/2). The peaks at higher binding energies, can be assigned to ruthenium species in higher oxidation states, as for example in RuO<sub>2</sub>.<sup>[34]</sup> A quantitative analysis of these signals indicates that the contribution of the oxidized species is of the order of 20%. Note that in order to have the surface chemistry information in conditions as close as possible to that corresponding to the catalysts used in the catalytic assays, the XPS data were recorded after the catalysts were exposed to air and without any further treatment inside the analysis chamber. Therefore, the presence of this small fraction of oxidized Ru must be related to surface oxidation of the small Ru nanoparticles.

The XP spectra of the same catalyst after reduction at 500 °C and 700 °C, as well as those corresponding to the other catalysts with lower Ru contents, show features similar to those just explained. Tables 2 and 3 provide additional quantitative data about the 1:0.7 AuRuCZ and 1:1.3 AuRuCZ catalysts, which allow understanding additional structural features of the prepared catalysts. Note that the Au:Ru atomic ratio values observed from XPS are in general lower than those determined by ICP-AES, thus indicating that the catalysts are Ru enriched at the level of the first surface layers. The values of the Inelastic Mean Free Paths (IMFP) for the Au 4f<sub>7/2</sub> and Ru 3d<sub>5/2</sub> electrons are 1.78 and 1.65 nm respectively. Therefore, the analysis depths of these two elements (about three times IMFP) are 5.3 and 5.0 nm respectively. This means that the atoms of any of the two metals at the core of nanoparticles with diameters larger than roughly 10 nm will be out of reach for this technique. Therefore, the deviations observed in the Au:Ru values with respect to the actual metal loadings suggest that Au in the bimetallic catalysts is in part present in the form of particles larger than those of Ru. In any case, to understand in more detail these Au:Ru ratios established by XPS and how other factors could contribute to these values it is first necessary to report the results of the Electron Microscopy studies.

## **2.2. Characterization at nanoscopic (STEM) and atomic (HREM) scales**

Electron Microscopy techniques, in both Transmission and Scanning-Transmission modes, have been used to unveil structural and compositional features of the investigated catalysts at atomic and nanoscopic scales respectively. Concerning the former, HREM images have been used both to reveal the atomic structure of the small metallic nanoparticles present in the catalysts as well as to determine their size. Information about particle size has been complemented from the analysis of HAADF-STEM images. On its hand, STEM-XEDS analysis using a very small, 0.5 nm, electron probe has allowed determining the chemical composition (Au:Ru molar ratio) of individual nanoparticles.

Before going into further details, it is necessary first to make some preliminary comments on the different imaging modes used in this Electron Microscopy investigation. HREM images, based on interference effects between coherently electron beams diffracted at low angles (below 20 mrad), provide images containing information on lattice planes distances and angles in the imaged areas, which can be used to monitor phase composition.<sup>[35]</sup> The metallic structures of Au and Ru are different. Au presents an fcc structure, whereas Ru crystallizes within an hcp type unit cell. This makes the HREM images of Au-rich and Ru-rich particles easily distinguishable from each other. Concerning the support, a very detailed analysis of HREM imaging in ceria-zirconia mixed oxides can be found in the literature.<sup>[36,37]</sup> In relation to the detectability limits of metallic nanoparticles supported on a heavy oxide, as it is the case of the  $\text{Ce}_{0.62}\text{Zr}_{0.38}\text{O}_2$  support used here, and the determination of their size a very detailed analysis can be found elsewhere.<sup>[37-41]</sup> In these studies the two most important imaging modes of supported nanoparticles are considered, i.e. profile- and top-view. In the former, the incoming electron beam runs parallel to the particle||support interface, in such a way that these two components are imaged separately on different areas and only in the region close to the interface information due to both components is expected to overlap. In top-view, the situation is quite different; the electron beam travels through both components. In this case, the electron beam exiting from the first component of the material (either particle or support) goes through the second and the information resulting from this complex two-step interaction process is stored in the same area of the image. This makes top-view imaging not only more complex but, at the same time, richer in terms of the information contained in the contrasts.<sup>[42]</sup> It is important to stress that this second type of imaging, top-view, is the most frequently found in the TEM/STEM images of supported catalysts, since in projection the image zones close to crystallite edges are much more limited than those corresponding to the image of the crystallites themselves .

Concerning the particular question of detection and size analysis of supported metal nanoparticles on ceria based oxides, previous simulation and experimental results point out that particles sizes as small as 0.5 nm can still be distinguished and safely measured in HREM images.<sup>[15,40]</sup>

In HAADF-STEM imaging, contrasts are related to the fraction of electrons in the incoming converging fine electron probe (subnanometer sized) scattered at very high angles.<sup>[43,44]</sup> The intensity at each point in these images is roughly related to the  $Z^2$  values of the atoms in the atomic columns. Therefore, in an area of constant thickness, these HAADF-STEM images will appear brighter in those locations in which heavy elements are present, higher values of  $Z$ , and with less intensity in those sites where light elements are located. In the case of the materials analyzed in this work the elements involved are: Ce ( $Z=58$ ), Zr ( $Z=40$ ), O ( $Z=8$ ), Au ( $Z=79$ ) and Ru ( $Z=44$ ). From these numbers, it is clear first that the contrasts in the oxide support crystallites will be dominated by the contribution of Ce and Zr,<sup>[36]</sup> given the large difference between the atomic number of these two elements and O. Likewise, it is clear that the intensity expected for the Au particles in these images is much larger than that corresponding to Ru. In a very rough estimate, an effective atomic number can be proposed for the support, just considering its stoichiometry in terms of Ce-Zr cations (62/38), which would provide a value of  $Z_{\text{eff}}=51$ . From this figure it appears that in the case of the metal nanoparticles imaged in profile view, the intensity in the areas of gold nanoparticles are expected to be brighter than those of the support, if the thickness of the support crystallites in the neighborhood is not too large and comparable to that of the metal nanoparticles. In the case of Ru, similar intensities should be expected, as long as the support is not too thick in the areas close to the nanoparticles. Of course, in the very thick areas of the support crystallites

the intensities of HAADF-STEM images must be very large, in comparison even with those of the Au nanoparticles.

Finally, the case of nanoparticles imaged in top-view in HAADF-STEM images is worth a more detailed comment. In this projection, the electrons scattered at high angles by the metal nanoparticles will add to those further scattered in a second step by the support crystallite underneath. Therefore, the total number of electrons scattered at high angles in the areas occupied by the supported nanoparticles should be higher than those in the close neighborhood of the nanoparticles. This additive effect would create a contrast difference between the area occupied by the metal nanoparticle and its surroundings, independently of the  $Z$  value of the metal nanoparticle being smaller or larger than the  $Z_{\text{eff}}$  of the support. This would provide a contrast mechanism to detect metal nanoparticles in plan view HAADF-STEM imaging for both Ru, with a  $Z$  number smaller than  $Z_{\text{eff}}$  of the support, and Au in which the case is just the opposite. This is clearly illustrated in the HAADF-STEM and HREM images included in **Figure S6** and **Figure S7**, recorded on the monometallic AuCZ and RuCZ catalysts. Note how both types of particles are observed in these images and that in the case of Ru, even relatively small ( $\approx 0.5$  nm) nanoparticles are detected. In any case, it is expected that the additive effect due to Au nanoparticles is much stronger than that due to Ru. This finally means that the expected detectable ultimate Ru metal particle size in HAADF images will be larger than that of Au nanoparticles. The latter should be detected in the form of much smaller particles on top of any support crystallite.

All these are possibly simplified arguments and additional imaging parameters should be considered in a more quantitative and detailed analysis of this topic (e.g. crystal tilts), but the images shown herein agree well with these qualitative considerations. In practical terms, the experimental analysis of supported metal systems indicates that the actual detection limit of

these nanoparticles (Au and Ru) is at least as good as 0.5 nm on ceria-zirconia crystallites in the 20-100 nm thickness range.<sup>[15,28]</sup> It is important to stress at this respect that the support used in this study was submitted to high temperature treatments and, consequently, the average support crystallite size is of the order of 50 nm.

### *2.2.1. Monometallic Catalysts Nanoparticle size distributions*

Figure S6 and Figure S7 shows representative HAADF-STEM and HREM images of the two monometallic catalysts reduced at increasing temperatures. Note how the metal nanoparticles can be clearly identified in both types of images. From the measurement of the diameter of a very large number of particles (>200) in these HREM and HAADF images, Particle Size (diameter) Distributions (PSDs) could be established for these catalysts, which are also shown on the right side of the Figures. In the monometallic catalysts activated at low temperature, 350 °C, the average particle size is small (1.4 nm and 2.4 nm for RuCZ and AuCZ respectively). Likewise, at least 90% of the metal nanoparticles are smaller than 5 nm in diameter. Note also that the two catalysts show a different sensitivity to sintering effects under the reducing environment. Clearly the AuCZ catalyst sinters to a much higher extent than RuCZ. In the former, increasing the reduction temperature from 350 °C to 500 °C leads to a clear shift of the PSD to larger particles sizes, a significant change in the average particle size (by 60%), and the appearance of a small fraction of very large (10 – 20 nm) Au particles. These effects are much more limited in the RuCZ-R500 catalyst, in which the average particle size increases by only 20% and all particles remain smaller than 8 nm.

Increasing the reduction temperature up to 700 °C amplifies the differences between these two catalysts. The AuCZ-R700 catalyst has a PSD spanning the 4-20 nm range, with an average Au particle size of 12 nm. In contrast, the PSD of the RuCZ-R700 catalyst still falls within the 0.5 – 8 nm range and the average Ru particle is just 2.2 nm in diameter.

Table 4, collects characteristic data calculated from the PSDs of the two monometallic catalysts. The dispersion,  $D$  ( $D=100*N_s/N_t$ ,  $N_s$ =number of metal atoms at the surface,  $N_t$ =total number of metal atoms) of the metallic phases is included. Note that the dispersion of the two monometallic catalysts reduced at the lowest temperature is of the same order, but the AuCZ catalyst losses a much larger fraction of dispersion at high temperatures than RuCZ. In the case of AuCZ, the dispersion loss takes place mostly at 500 °C whereas in the case of RuCZ at least 700 °C are necessary to modify the dispersion of the Ru particle system.

### 2.2.2. Bimetallic Catalysts

**Figures 4(a) - 4(c)** show representative HAADF-STEM images, roughly at the same magnification, of the 1:0.7 AuRuCZ bimetallic catalyst reduced at increasing temperatures. Note how the density of small particles is maintained between 350 °C and 500 °C but it diminishes significantly after reduction at 700 °C. The particle size information related to this bimetallic catalyst is gathered in Figures 4(d) – 4(f) and Table 5. The PSDs shown in these Figures and the corresponding data in Table 5 take into account the whole set of particles, independent of their chemical nature.

The PSDs of the bimetallic catalyst after reduction at 350 °C and 500 °C resemble those of the pure gold catalyst after the same treatments. The percentage of particles larger than 5 nm has increased slightly and the differences in the average particle sizes between these two sets of samples are of 1 nm or below. These results suggest that the incorporation of Ru has only slightly modified the size of the initial set of particles present in the monometallic AuCZ catalyst. As shown in **Figure 5**, STEM-XEDS analysis of individual particles in these catalysts indicates the presence of both pure (Au and Ru) as well as bimetallic nanoparticles. It is also very important to indicate that after reduction at 500 °C the bimetallic catalyst do not

contain particles larger than 10 nm in diameter, as those observed in small amounts in the AuCZ monometallic. This result points out towards a moderation of the sintering process of Au in the 1:0.7 AuRuCZ bimetallic.

After reduction at 700 °C, the PSD of the bimetallic catalyst becomes very wide and shows a distinct feature, the presence of a higher fraction of particles in the 1-5 nm size range, which is not observed in the monometallic AuCZ. As it will be shown later, a fraction of these smaller particles correspond to tiny Ru nanoparticles, which have not suffered sintering, as it occurs in the monometallic RuCZ catalyst. The average particle size of the 1:0.7 AuRuCZ-R700 catalyst is 7.9 nm, i.e. lower than that of the AuCZ catalyst after the same treatment. As it was also observed in the bimetallic catalyst reduced at 500 °C, the contribution of particles larger than 10 nm ( $\approx 30\%$ ) is much lower than in the monometallic AuCZ catalyst ( $\approx 55\%$ ) after reduction at 700 °C.

The dispersion of the initial 1:0.7 AuRuCZ-R350 catalyst (28%) is smaller than that of the gold monometallic (41%). Nevertheless, in comparison with the AuCZ catalyst, the decrease of dispersion after reduction at 500 °C is negligible in the bimetallic, maintaining a value close to 30%. After reduction at 700 °C, the dispersion in the bimetallic,  $D=11\%$ , reaches the same value than in the AuCZ reference catalyst, in spite of the difference in average particle size between them. This is so because the parameter  $D$  is dominated by the contribution of large particles, whose percentages are high in both catalysts. This result stresses also the importance of knowing the whole PSDs, rather than just average particle size values (as those determined by XRD), to characterize the surface properties of this type of catalysts.

**Figure 6** shows a set of HAADF-STEM and HREM images representative of the bimetallic with medium Ru content, 1:1.3 AuRuCZ, after reduction at different temperatures. Note how

in this case, especially in HREM images, a very large number of small nanoparticles are observed after reduction at 350 °C and 500 °C. Accompanying these small nanoparticles, a few larger aggregates are also visible. Likewise, as previously commented for the 1:0.7 AuRuCZ catalyst, reduction at 700 °C provokes a significant decrease in the surface density of nanoparticles in this catalyst. Effectively, in Figure 6(c) the number of nanoparticles per unit area has clearly decreased. These changes are better observed in the PSDs shown as Figures 6(g) – 6(i). In this catalyst the PSD corresponding to the sample activated at the lowest reduction temperature appears clearly bimodal, with a set of particles with an average size around 2.1 nm and a second set with a 5.7 nm average diameter. Particles of the first set are those observed in large number in the HREM images. The analysis of high magnification HREM images, as that shown in **Figure 7(a)**, indicates that these are mostly Ru-rich nanoparticles. Digital Diffraction Patterns (DDPs) of the HREM images corresponding to areas occupied by these nanoparticles, show (002) and (101) hcp Ru reflections. Moreover, the (002) planes lie parallel to the (111) planes of the Ceria-zirconia support, clearly suggesting an orientation relationship in the growth of the Ru nanoparticles on the surface of the oxide support. The sixfold type symmetry characteristic of these two planes of metal and support is possibly at the roots of this particular type of growth. Note also that the stacking of just a few, 3-4, (002) Ru planes makes up these small particles. Direct chemical analysis of nanoparticles in this size range, by STEM-XEDS, also confirms this point, as shown in Figures 7(b)-(c).

Analysis of the larger nanoparticles has shown the presence of bimetallic entities, **Figure 8**. An XEDS analysis performed along the path marked with an arrow on the HAADF image of the supported nanoparticle indicates that Ru is not uniformly distributed in the bimetallic nanoparticles but it is, instead, localized in small areas. Thus, in this 9 nm in diameter particle, Au is identified along the entire analysis path, which runs through the whole diameter,

whereas Ru is only detected in a region (marked with an asterisk on the HAADF image) about 2 nm in size. The average Ru content of the nanoparticle is 2 at.%, but locally the Ru concentration rises, as observed in the plot, up to 35 at%. The detection of Ce and Zr indicates that the particle overlaps the support at the final stretch of the path.

In good agreement with the behavior observed in the catalyst with the lowest Ru content, increasing the reduction temperature up to 500 °C, only slightly modifies the PSD, which still appears bimodal with average diameters at 2.0 nm and 5.8 nm. Nanoanalysis performed on different nanoparticles reveals the nature of the bimetallic particles present in these catalysts, **Figure S8**. The HAADF-STEM image shows in this case a large metallic aggregate, about 20 nm in diameter, on top of whose surface a very small ( $\approx 2$  nm) particle is observed. XEDS analysis performed at the points marked by 1 and 2 reveal that the large aggregate is made up of Au whereas the small nanoparticle contains mostly Ru. This result indicates that the bimetallic entities are formed by decoration of the surface of the preexisting Au nanoparticles with Ru-rich nanodomains rather than by the formation of alloy type particles. This result is also in good agreement with the XEDS analysis presented in Figure 8, where this type of particle association would be imaged in top-view. The low miscibility gap between Ru and Au,<sup>[45]</sup> as well as the synthesis method used, based on preformed Au nanoparticles and relatively low activation temperatures are also in line with the observed results.

Reduction at 700 °C in 1:1.3 AuRuCZ-R700 catalyst, merges the two parts of the bimodal distribution together, Figure 6(i), giving rise to a PSD with an average diameter of 5.5 nm and, though still small in number, a higher contribution of large particles (10 – 20 nm).

Finally, **Figures 9(a) – 9(i)** show a collection of HAADF and HREM images representative of the changes with reduction temperature of the bimetallic catalysts with the lowest Au:Ru ratio, 1:2.4. Note how now a significant fraction of particles with diameters in the 2-3 nm range are

clearly visible. From the DDPs, both particles with fcc (Au) and hcp (Ru) structures can be detected at the three reduction temperatures, **Figure S9**. Direct XEDS analysis of individual nanoparticles detects the presence of the three types of particles observed previously, i.e. Ru, Au, and AuRu bimetallics, **Figure S10**.

The PSD corresponding to the 1:2.4 AuRuCZ-R350 catalyst, Figure 9(g), looks again unimodal, this suggesting, in good agreement with XRD, that the average size of the Ru nanoparticles has increased to a value close to that of the Au nanoparticles. The average particle size of 2.5 nm is close to the value of the smaller set of nanoparticles in the bimodal distribution of 1:1.3 AuRuCZ-350. As it happened also with this last catalyst of medium Ru content, reduction at 500 °C does not modify significantly neither the PSD, Figure 9(h), nor the average particle size value or the dispersion of the 1:2.4 AuRuCZ catalyst.

Once more, increasing reduction temperature up to 700 °C, gives rise to the more dramatic changes in the system of nanoparticles in the 1:2.4 AuRuCZ catalyst. The PSD shows after this treatment a significant, more or less continuous, tail of large diameter particles. This, along with a small shift of the major body of the distribution to larger diameters, results in an average diameter of 4.4 nm. STEM-XEDS allowed identifying in this catalyst the presence of large Au and Ru particles, Figure S10.

Concerning Dispersion, as it was also the case with the 1:1.3 AuRuCZ catalyst, the initial 1:2.4 AuRuCZ-R350 catalyst shows lower values than the monometallic AuCZ, 26%. The value does not change after reduction at 500 °C but drops down to about a half when the catalyst is reduced at 700 °C, Table 5.

### *2.2.3 HAADF-STEM tomography*

The two monometallic catalysts as well as the bimetallic with the highest Ru content were characterized by HAADF-STEM tomography. Tilt series were acquired for these three catalysts and after their alignment, the reconstructions were performed using the “Simultaneous Iterative Reconstruction Technique” (SIRT) with 25 iterations. Visualizations of the 3-D reconstructed volumes of the catalysts are shown in Figure 10. So-called “orthoslices” through the 3D reconstructions indicate that all the metal nanoparticles are located at the surface of the support crystallites, as marked in Figure 10 b), d) and f).

After the segmentation of the reconstructed volume, the metal particles could be separated from the ceria-zirconia support. From the volume of each segmented nanoparticle, the diameter could be determined. The PSDs determined from 3D information are shown in **Figure S11**. As indicated, the number of particles included in these PSDs is much lower, especially in the case of the RuCZ-R350 monometallic in which the lower contrast of the very small nanoparticles hampers their detection.

The average diameter determined for the AuCZ-R350 (2.4 nm) and 1:2.4 AuRuCZ-R350 (2.5 nm) catalysts coincide exactly with those determined on the basis of a much larger number of particles by 2D imaging techniques. In the case of the monometallic RuCZ-R350 (2.1 nm) there is a deviation to larger values. The statistics in this case are much poorer (just 8 particles in the distribution) but note that most of them (75%) present a diameter (1.5 nm) very close to that determined by 2D imaging.

In summary, the electron tomography analysis validates the results determined by 2D HREM and HAADF-STEM.

#### 2.2.4 Comparison of XRD and STEM data

For a more detailed analysis of the influence of both Ru loading and reduction temperature on the size features of the system of particles present in the different catalysts, a quantitative comparison was made between data obtained by macroscopic analysis, i.e. XRD diagrams, and nanoscopic techniques (HREM, HAADF). For a meaningful comparison between these techniques, the average crystalline domain size values determined by the Scherrer approximation need be compared with those corresponding to the volume averaged diameters of the PSDs determined by (S)TEM. These values have been gathered in Table 5. A very good agreement is observed between these two very different approaches, with differences of the order of 1 nm. The difference is larger for the catalyst with the highest Ru content. In this case, we have to consider that the contribution to the XRD peaks comes mostly from Au, whereas PSDs established by STEM take into account in a greater detail the contributions of both Ru and Au. The Ru particles are rather small and make the STEM determined value smaller than that obtained by XRD. In fact the difference in the case of the 1:2.4 AuRuCZ-R350 catalyst, in which Ru particles are still small, is larger (6 nm) than in the 1:2.4 AuRuCZ-R700 catalyst, in which Ru particles have already become rather large.

This result indicates that the PSDs distribution established by STEM can be considered representative of the state of the catalysts at a macroscopic level.

A second question worth commenting refers to the influence of Ru addition on the size characteristics of the system of particles. Two effects are clearly observed at this respect. First in the initial catalysts, those reduced at 350 °C, the addition of Ru gives rise to a larger average diameter with respect to the monometallic AuCZ reference. Only when the amount of Ru is very high, and the contribution of small Ru particles becomes very important, in 1:2.4 AuRuCZ-350C, the average diameter comes close to that of the AuCZ monometallic. These results suggest that the addition of Ru gives rise to an increase of the diameter of the Au-rich

fraction of the distribution. This increase is compensated to a different extent by the contribution of very small Ru-rich nanoparticles. Thus in the two bimetallic catalysts with lower Ru loadings, the balance translates into an average diameter larger than in the AuCZ monometallic, whereas it gives rise to a smaller average value in the catalyst with the highest Ru loading.

Though this last observation will be further analyzed in the following section with additional data, it is important to stress that the preparation of AuRu bimetallics by alternative routes gives rise to similar results. Figures S12 to S14 provides structural information concerning these Au-Ru catalysts prepared by alternative routes. In particular, **Figure S12** shows HAADF and XEDS-STEM data obtained on a AuRu catalyst which was prepared adding Ru by DP on a Au catalyst previously prepared also by DP. Note how in addition to very small nanoparticles seen in the HAADF-STEM image in **Figure S12(a)**, there are also large aggregates, seen in **Figure S12(b)**, which are made up of Au, as revealed by the composition profile determined by XEDS-STEM (inset). This gives rise to a catalyst exhibiting a very wide PSD and a very poor metal dispersion ( $D=6\%$ ). If the starting Au monometallic catalyst prepared by DP is calcined prior to the addition of Ru by DP, the resulting system of particles presents a narrower PSD, **Figure S13**, but still both the average particle size, 5.3 nm, and the width of the PSD distribution (0.5-17 nm) are much higher than those of the starting AuCZ catalyst. If the two metals are added in the reverse order, i.e. first Ru (incorporated by impregnation) and then Au (added by DP), the results are also similar, **Figure S14**. In this case, STEM data have shown the occurrence of very large (close to 100 nm) metallic particles, **Figures S14(a)** and **S14(b)**, made up of Au (see XEDS-STEM data shown as inset).

Finally, it is also important to comment on the effects of Ru on the resistance of the bimetallic catalysts against to sintering in the family of bimetallic catalysts prepared in this study. In this respect, the comparison of the average diameter data corresponding to the bimetallic catalysts treated at 500 °C and 700 °C with those of the AuCZ monometallic suggests that Ru limits the growth of the system of particles at high temperatures. The most remarkable feature is that increasing additions of Ru gives rises to decreasing contributions to the PSDs of the fraction of larger particles sizes. Nevertheless to discuss in more detail this question, additional data presented in the next section are necessary.

#### *2.2.5. Detailed Nanoanalytical studies: Composition-size relationships*

To understand in more detail the structure of the system of nanoparticles, a comprehensive analytical study of individual nanoparticles present in the different catalysts was undertaken following the approach by Lyman et al.<sup>[24,25]</sup> In this study, at least 75 nanoparticles were analyzed on each sample. **Figure 11** gathers the results of this study for the bimetallic catalysts with the three varying Ru loadings. Two types of information are shown: composition (Ru at.%) versus particle size plots and percentage of particle types (Au, Ru and AuRu bimetallics irrespectively of their composition). Information extracted from these data, complements and clarifies the comments previously made on the basis of the PSDs and XEDS data presented in the previous section. In particular, it is possible to discriminate in more detail the evolution, with Ru loading and reduction temperature, of the dimensions of each type of particle. Likewise, average composition of the bimetallics can be tracked.

Note first that, in all cases, events of the three types of particles, Au-rich, Ru-rich, and AuRu bimetallics, are present in all the catalysts, which gives this type of materials a complex nanostructure. A number of parameters have been estimated from the composition-size plots,

which are gathered in Table 6. In particular the size range of each type of particle, their average size and the average Au content in the case of the bimetallics are presented.

From the plots in Figure 11 and the data in Table 6 it is clear that the Ru-rich particles are those covering the small size range, especially in the catalysts treated at 350 °C. Only the catalyst with the highest Ru loading after reduction at the highest temperature contains large Ru particles. Apart from this later sample, the average size of Ru nanoparticles is much smaller than those of Au or bimetallics in most catalysts. In comparison, Au rich nanoparticles cover the large end of the size range. AuRu bimetallics cover a size range similar to that of Au particles and their average size lies in most cases at an intermediate value between those of the pure components. These observations are in good agreement with the HREM and XEDS-STEM data reported in the previous section.

The Ru particle size in the bimetallic catalysts is similar to that of the monometallic for the two lower loadings. As indicated in Table 1, the total amount of this metal is smaller in the bimetallics. When the amount of Ru is of the same order in the bimetallic as in the pure catalyst, the Ru particles are slightly larger after reduction at 350 °C and 500 °C but much larger after reduction at 700 °C. This result indicates that the presence of gold deteriorates the sintering resistance of Ru.

In the case of gold particles, all the average values observed after reduction at low temperature, 350 °C, are well above that in AuCZ-R350 monometallic. This clearly indicates, as already discussed in the previous section, that the incorporation of Ru gives rise to the growth of the initial system of Au nanoparticles. In spite of this first effect, Ru also plays a role as a dispersion stabilizer against treatments at very high temperatures. Note at this respect

that the average size values of both the Au and the bimetallics in all the catalysts reduced at 700 °C are below that in the pure AuCZ-R700 monometallic.

The average composition of the bimetallic catalysts is in general very rich in Au and their size behavior resembles that of the pure Au particles. In general, the Au content in the bimetallic nanoparticles ranges from 80 – 90 at.%. In the catalysts with considerable amounts of Ru, increasing reduction temperature increases the Ru content of the bimetallic nanoparticles.

Another question which can be answered from data in Figure 11 is the fraction of the different types of particles in each sample as well as the expected Au:Ru ratio. For the later value, a particular morphology must be assumed for the nanoparticles (e.g. truncated cuboctahedron or hemisphere). Figure 11 and Table 6 display this information. It is important to stress first that the Au:Ru ratios determined from the nanoanalytical study are much higher than those determined by ICP-AES. This indicates that in the STEM-XEDS study the selection of particles concentrated on the Au-containing phases.

This bias to Au-rich nanoparticles is not related to the un-detectability of the Ru particles, since we have already shown HREM and HAADF images in which small Ru and Ru-rich nanoparticles were detected. Difficulties with the Au:Ru ratio determined from STEM-XEDS arise from the following factors instead:

- (1) Ru particles are much smaller than Au-containing nanoparticles. This means that to arrive at an analytical study representative of the average composition a much higher number of Ru-containing nanoparticles must be analyzed. For example, if the average size of Ru particles is about 2 nm and that of the Au particles is about 6 nm, the number of Ru particles that should be analyzed should be at least 27 times the number of analyzed Au particles in the case of a

catalyst with 1:1 molar ratio. This would go to roughly 20 times or over 50 times in the cases of 1:0.7 and 1:2.4 molar ratios as it is our case. If the number of analysis of the Au rich particles needs to be representative, the required number of analyses of Ru-rich particles reaches unacceptable values.

(2) Three microscope technique factors complicate the analysis of Ru containing particles. They show much lower contrast in HAADF images, thus increasing the difficulty for their selection during the nanoanalytical studies. They are also more sensitive to damaging under the electron beam and, finally, the signal to noise (S/N) ratio in these particles is smaller. In other words, a fraction of the Ru particles selected for analysis will render useless spectra due to very poor S/N ratios or beam damage, which in turn increases further the ratio of Ru/Au particles to be analyzed.

From the nanoanalytical results, PSDs can be also determined which consider all the measurements performed on each catalyst. Chemically sensitive PSDs established from the nanoanalytical studies of the three catalysts reduced at 350 °C are shown in **Figure 12**. Note first the large difference in the number of particles measured with each technique. In the case of imaging techniques the total number of measured particles is about 500 or above, whereas it is one order of magnitude smaller in the case of STEM-XEDS measurements. Note also that the major difference between the two sets of PSDs is the contribution of particles in the very small size range (< 3 nm). These particles represent up to 50% in the PSDs of the 1:0,7 AuRuCZ-R350 and 1:1.3 AuRuCZ-R500 catalysts, and up to 75% in the 1:0.7 AuRuCZ-R700 as determined by HREM and HAADF. In contrast particles analyzed by XEDS in this size range represent only about 25%. This is the size range where most Ru particles are found, clearly explaining the large underestimation of the Ru content by XEDS-STEM.

Therefore, factors due to both the nature of the samples and inherent technical difficulties are at the roots of this deviation. In any case it is not a problem of detection of small particles in the analytical studies since Figure 11 contains in fact events corresponding to pretty small Ru nanoparticles.

Taking into account this limitation in the nanoanalytical studies, it becomes clear that parameters like the average size, size range and average composition of the bimetallics can be considered as very reliable, whereas the absolute frequency of each type of particle can be affected by large errors. Since STEM data point out a type of bimetallic particles made up of aggregations of smaller monometallic domains, it would be expected that increasing either the Ru content or the reduction temperature should increase the fraction of bimetallic particles present in the system. This is in general what it is observed in the set of data in Table 6. These data clearly fulfill the expectations derived from the observations by imaging techniques. Therefore, the nanoanalytical study performed here does not provide accurate absolute values of the percentages of monometallic and bimetallic particles present in each catalyst but it correctly captures their relative amounts as a function of both Ru loading and reduction temperature.

Table 7 shows the values of Ru molar contents for the three AuRuCZ-R350 catalysts as determined by ICP-AES, XPS and STEM-XEDS. The presence of a large fraction of highly dispersed Ru nanoparticles is responsible for both, a much larger fraction of Ru in the XPS data and, at the same time, the large underestimation of Ru in the STEM-XEDS study. Moreover, the values of the Au:Ru molar ratios determined by XPS cannot be fully taken into account by the relative sizes of the Ru and Au-rich nanoparticles, so some additional factor must be operating. To this respect, STEM data suggest that Ru particles decorate the surface

of gold ones. Since these particles are a few nanometers in diameter, this shielding effect must be also contributing to the Au:Ru ratios observed by XPS.

### **2.3. Catalytic activity in octanol oxidation**

Table 8 gathers the activity and selectivity towards 1-octanal values measured after three hours of reaction time over the monometallic and bimetallic catalysts reduced at 350 °C. In all cases the selectivity towards the desired product is above 99%, the differences between the catalysts being established in terms of activity. Given the differences in total metal loadings, intrinsic catalytic activities per exposed metal atom (Turn Over Frequencies or TOF) after 30 minutes of reaction were estimated, Table 8. For this calculation, the total dispersion, with independence of the nature of the exposed metal atom, and total metal molar loadings were considered. The TOF values of the two monometallic catalysts are very similar. To the best of our knowledge this is the first example where Au and Ru catalysts show a similar activity in this reaction. Indeed previous studies reported that Ru is significantly more active than Au when supported on activated carbon, which is in fact not active.<sup>[16]</sup> It is clear that ceria-zirconia mixed oxide is able to promote the activity of Au in the oxidation of alcohols.<sup>[9]</sup> This result also points out that, when supported on  $\text{Ce}_{0.62}\text{Zr}_{0.38}\text{O}_2$ , the intrinsic activity of a Ru metal atom is roughly equivalent to that of a Au atom. This fact simplifies the analysis of the rest of the activity data. It seems clear from these results that the simultaneous incorporation of the two metals on the ceria-zirconia support increases the intrinsic activity of the exposed metal atoms, this proving the occurrence of synergistic effects between the two metals. This result is in good agreement with previous reports in the oxidation of glycerol and octanol.<sup>[15-17]</sup>

Table 8 also indicates that the synergy between the two metals increases with Ru content. Information provided by STEM imaging techniques suggests that these synergies must be

related to the appearance of new active sites at the contact areas between the nanodomains integrating into the bimetallic nanoparticles. It is important to stress that H<sub>2</sub>-TPR results indicate a chemical interaction between the two metals.

The nanoanalytical study reported in Table 6 suggests as the Ru content is increased an increasing fraction of bimetallic nanoparticles occurs in the series of bimetallic catalysts reduced at 350 °C. This result agrees with the increasing activity observed with Ru loading.

In summary, the nanostructural study provides some clues to understand the general trends observed in the catalytic performance but more details about the exact nature of the active sites for this reaction on this type of catalyst is out of reach on the basis of the available catalytic and characterization data.

### **3. Conclusions**

A series of gold-ruthenium bimetallic catalysts supported on a ceria-zirconia mixed oxide, Ce<sub>0.62</sub>Zr<sub>0.38</sub>O<sub>2</sub>, with improved redox properties has been prepared and their structural and chemical features characterized by a combination of macroscopic and atomic scale techniques based on Scanning Transmission Electron Microscopy (STEM). While the total Au content was kept constant in the whole series, increasing amounts of Ru were considered, to check the influence of changing the Au:Ru ratio. Likewise, the influence of the temperature of the final reduction treatment used as activation step (350 °C – 700 °C range) has also been established. From High Resolution Electron Microscopy (HREM) and High Angle Annular Dark Field STEM (HAADF-STEM) images the size distribution of the metal particles present in each catalyst was determined. These distributions provided data agreeing with macroscopic X-Ray Diffraction (XRD) results. Moreover, our analysis indicates that both techniques, HREM and HAADF-STEM, are required in this particular type of systems to determine, on a

reliable basis, the particle size distributions. The average diameter of the system of metal nanoparticles in the bimetallic catalysts reduced at the lowest temperature (350 °C) is below 4 nm, independent of the Au:Ru ratio. In fact, roughly 80% of the metal nanoparticles in these catalysts have diameters under 5 nm, which means that the employed synthesis procedure allowed us to prepare well-dispersed systems. PSDs established from 3D information obtained using HAADF-STEM electron tomography confirmed the information about particle size distribution established by conventional 2D microscopy techniques.

As expected, increasing the reduction temperature leads to a growth of the metal particles by sintering. A comparison with the behavior of a monometallic gold catalysts of the same total Au loading demonstrates that the incorporation of Ru in the bimetallic catalysts results in a small increase of the average size of the initial system of gold particles but it also clearly limits the effect of metal sintering; this clearly revealing that Ru stabilizes the dispersion of Au against high temperature treatments.

The determination of the composition (at. %Au) of a large number of individual nanometer sized nanoparticles, by STEM X-Ray Energy Dispersive analysis (STEM-XEDS), allowed identification of three different types of particles in all the catalysts: monometallic Au and Ru particles as well as bimetallic ones, of varying Au:Ru molar ratios. Bimetallic particles as small as 0.5 nm in diameter were detected. Particle size / composition diagrams have been established for all the catalysts, which suggest that increasing either the Ru content or the reduction temperature gives rise to a higher fraction of bimetallic particles. Likewise, STEM-XEDS analyses performed under conditions of very high spatial resolution prove that the bimetallic nanoparticles are in fact formed by decoration of the surface of gold nanoparticles with smaller, 3D, Ru nanodomains.

A comparison of quantitative data calculated from the composition/size diagrams and models for the metal particles with those obtained by macroscopic techniques, as Inductively Coupled Plasma – Atomic Absorption Spectrometry (ICP-AES) or X-Ray Photoelectron

Spectroscopy (XPS), reveals limitations of the nanoanalytical studies in providing accurate absolute values for the percentage of the different types of particles present in this type of complex systems. Thus, both XPS and ICP-AES results indicate that STEM-XEDS studies clearly underestimate the fraction of pure, very small (0.5-1 nm), Ru particles present in this type of catalysts. This underestimation is mainly due to the intrinsic characteristics of the system of metal particles present in the catalyst, which is dominated by a large fraction of very small Ru nanoparticles (< 2 nm) but also due to difficulties of their analysis using STEM.

The results of catalytic assays in the oxidation of octanol in liquid phase at 80 °C on the prepared catalysts indicate the occurrence of a synergistic effect between Au and Ru in the bimetallic catalysts, which increases with decreasing Au:Ru ratio. In particular, the catalyst with the lowest Au:Ru ratio, 1:2.4, showed the highest intrinsic activity per metal atom exposed at the surface (TOF). Such an enhancement of the intrinsic activity correlates with the formation of bimetallic nanoparticles. The high spatial resolution STEM-XEDS results suggest that this synergy must result from the appearance of new sites at the boundaries between the Au-Ru contacts created on the bimetallic aggregates.

Also quite remarkable, the selectivity to the desired oxidation product in this reaction, octanal, was above 99% on all the bimetallic catalysts.

Finally, the whole set of characterization data reveal the need to rely on the simultaneous use of complementary macroscopic and microscopic techniques to accurately reveal the complex structure of this type of systems, consisting of a mixture of different type of particles whose size range and compositions change as a function of both the molar ratio of the two metals involved and the activation conditions of the catalyst. Though nanoscopic and atomic scale techniques provide unique information about the structural and compositional features of individual particles and their mutual interactions, that are out of reach for macroscopic techniques, they have to be combined with these to draw an accurate and

representative picture of the surface structure of the bimetallic catalyst which is, relevant to understand their catalytic performance.

#### 4. Experimental Section

*Catalyst preparation:*  $\text{Ce}_{0.62}\text{Zr}_{0.38}\text{O}_2$  oxide provided by Grace Davison ( $20\text{m}^2\text{g}^{-1}$ ) was used as the support. In order to enhance its reducibility, this oxide was submitted to successive ageing cycles consisting of a severe reduction treatment (SR) followed by a mild oxidation step (MO).<sup>[29,30]</sup> 50g of  $\text{Ce}_{0.62}\text{Zr}_{0.38}\text{O}_2$  oxide was first reduced in a flow of pure hydrogen at  $950\text{ }^\circ\text{C}$  (5 h), flushed with helium at  $950\text{ }^\circ\text{C}$  (1 h), and then cooled to room temperature (RT) under inert gas flow. After completing this severe reduction step, the support was reoxidized at RT with pulses of helium-oxygen mixture (5% $\text{O}_2/\text{He}$ ) and later on was heated under the same gas flowing at  $500\text{ }^\circ\text{C}$  for 1 h. In all steps a flow rate of  $500\text{ ml min}^{-1}$  and a heating rate of  $5\text{ }^\circ\text{C min}^{-1}$  were used. The resulting oxide will be further referred to as CZ.

The comparison of the TPR-MS profiles for the starting (CZ-LS) and aged (CZ) materials presented in the Supporting information (**Figure S2a,b**), clearly shows that the SRMO pretreatment enhances the low-temperature reducibility of the CZ mixed oxide sample. This observation is in good agreement with previous investigations of such materials.<sup>[29,30]</sup> The different redox behavior of CZ oxide has been correlated to the presence of pyrochlore-related ordered cationic sub-lattice structures, which were identified in the CZ sample. The CZ support was used to prepare a monometallic 1wt.% gold catalyst, AuCZ, using the standard deposition-precipitation procedure as previously reported.<sup>[46]</sup> The final mixture was allowed to dry in an oven at  $110\text{ }^\circ\text{C}$  overnight and oxidized at  $250\text{ }^\circ\text{C}$  in helium-oxygen mixture ( $\text{O}_2(5\%)/\text{He}$ ) for 1 hour and then cooled under the same flowing. The obtained gold catalyst was used as a precursor for the preparation of a series of bimetallic AuRuCZ catalysts varying the ruthenium content. Three ruthenium solutions were prepared at different concentration by dissolving  $\text{Ru}(\text{NO})(\text{NO}_3)_3$  (Alfa Aesar, 99.9%) in 10 ml of distilled water. Then 1ml of Ru-

containing solution was added to 3 g AuCZ catalysts. After the impregnation, the catalysts were dried at 110 °C for 12 h followed by reduction treatment at 350 °C in pure hydrogen flow (1h) followed by flushing helium at same temperature (1h) and then cooled under the same flowing in a cooling bath mixture (liquid nitrogen/acetone) for 30 min. A 1wt.% ruthenium monometallic catalyst for comparative purposes was prepared at the same manner describe above using the wetness impregnation method and submitted to a reduction treatment at 350 °C.

*Samples characterization:* Gold and ruthenium loadings were determined by means of inductively coupled plasma atomic emission spectrometry (ICP-AES). 20 mg of each catalyst was dissolved in aqua regia followed by microwave digestion and diluted in ultrapure water. The measurement was performed with a Iris Intrepid instrument (Thermo Elemental).

Specific surface areas were determined using Micromeritics ASAP2020 apparatus. Before the analysis, all samples were degassed for 12 h at 200 °C. Adsorption and desorption of nitrogen measurements were performed at -196 °C. Measurement of the specific surface areas were performed by multipoint on basis of the BET (Brunauer-Emmet-Teller) theory and equation.

The X-ray diffraction (XRD) profiles were collected from 10 to 100 2 $\theta$  at a 0.05° in step size and step time of 30 s using a Bruker AXS D8 Advance X-Ray diffractometer operating with Cu-K radiation source ( $\lambda$  average = 1.5418 Å) operated at 40kV and 40 mA.

X-ray photoelectron spectroscopy (XPS) measurements of all samples were acquired on a Kratos Axis Ultra DLD spectrometer. The samples were mounted as pellets using double-sided adhesive tape. Spectra were recorded by using monochromatized AlK $\alpha$  radiation (1486.6 eV) at a power of 150 W, in constant analyzer energy (CAE) mode, with pass energy of 20 eV. Surface charging effects were compensated by using the Kratos coaxial neutralization system. The binding energy (BE) scale was referenced to the Zr 3d<sub>5/2</sub> (182.64 eV) component present in the mixed oxide support<sup>[32]</sup>. Quantitative chemical surface analysis

was based on XPS peaks areas determined by XPSMultiQuant v. 7.00.92 software (Dr. M. Mohai, Hungarian Academy of Sciences). Due to the overlap of the C 1s peak (coming from adventitious carbon contamination) with the Ru 3d<sub>3/2</sub> peak, for quantitative analyses the Ru 3p peaks were better chosen, and compared with corresponding Au 4f peaks to estimate Au:Ru molar ratios.

Samples suitable for transmission electron microscopy analysis were prepared by dry deposition of the catalyst onto holey carbon copper grids. HREM and STEM images together with compositional analysis by STEM-XEDS (X-ray energy dispersive spectroscopy) were performed in a JEOL 2010F FEG transmission electron microscope equipped with an Oxford Instruments X-Max large area Silicon Drift Detector (SDD) spectrometer with an active area of 80mm<sup>2</sup> for analysis. The XEDS data were collected with a probe of about 0.5 nm, an acceleration voltage of 200 kV. Atomic fraction of gold and ruthenium were quantified from intensities of Au-L (at 9.71 keV) and Ru-K (at 19.29 keV) series using the Cliff-Lorimer theory. High resolution STEM imaging and tomography experiments were performed in a FEI Titan 80-50 microscope operated at 300 kV. Digital Micrograph and TIA software were used for the analysis of TEM micrographs. For the tomography experiments the samples were tilted about a single axis with respect to the electron beam using a Fischione model 2030 single tilt tomographic holder. To reconstruct the tomograms, the registered tilt series were aligned using the FEI Inspect 3D. The reconstruction was performed by using the Simultaneous Iterative Reconstruction Technique (SIRT).

*Catalytic activity:* The activity of the catalysts for octanol oxidation was conducted in a thermostated glass reactor (30mL capacity) equipped with an electronically controlled magnetic stirrer and connected to a 5000 mL reservoir containing oxygen (300 kPa). The oxygen uptake was followed by a mass flow controller connected to a PC through an A/D board, plotting a flow versus time graph. 1-octanol and the appropriate amount of catalyst were mixed in the solvent (octanol/toluene at concentration of 10/90 volume/volume) in order

to reach a concentration of 100 mol of alcohol/1 mol of total metal (active phase). After the catalyst was loaded, the reactor was pressurized at 300 kPa of oxygen and heated under moderate agitation until 353K. Once this temperature was reached, an initial liquid sample was removed to mark the start of reaction. The reaction course was controlled during the 3 h reaction time by taking samples (0.5 ml) at regular time intervals and analyzing them by gas chromatography (GC) using a HP 7820A chromatograph equipped with a capillary column HP-5 (30m x 0.32 mm x 0.25 mm film thickness), a thermal conductivity detector (TCD) and a flame ionization detector (FID), by Agilent Technologies. Quantification of the reaction products was done by the external calibration method. TOF were calculated according to the following expression:

$$\text{TOF}(\text{h}^{-1}) = (\text{Conversion} / 100) \cdot n_{\text{alcohol}} / t \cdot n_{\text{metal}} \cdot D$$

### **Supporting Information**

Supporting Information is available online from the Wiley Online Library or from the author.

### **Acknowledgements**

This work has been supported by the Ministry of Science and Innovation of Spain/FEDER Program of the EU (Project: MAT 2013-40823-R, CSD2009-00013), ESTEEM2 (FP7-INFRASTRUCTURE-2012-1-312493), Junta de Andalucía (FQM334 and FQM110 and Project: FQM3994). S.B. acknowledges the European Research Council, ERC grant N°335078 – Colouratom. M.K. is grateful to the Fund for Scientific Research Flanders.

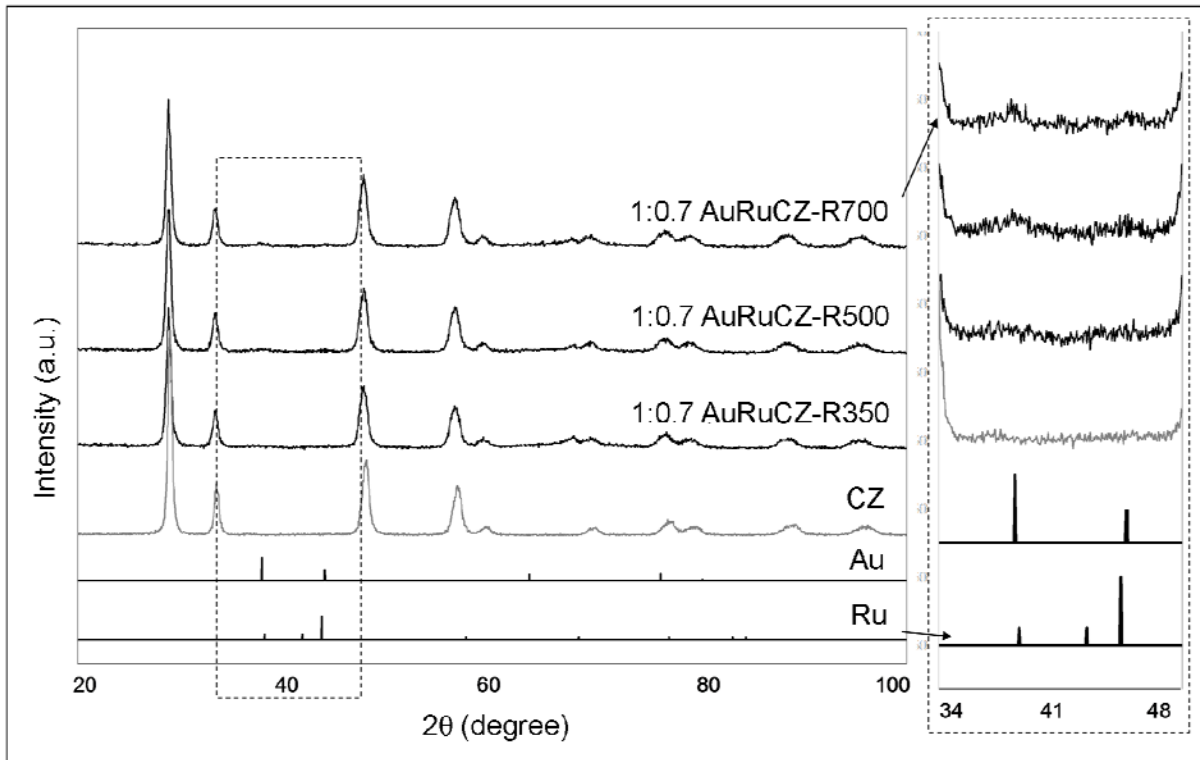


**Figure 1.** X-ray diffraction patterns of 1:0.7 AuRuCZ reduced at increasing temperatures. The insets show enlarged diagrams.

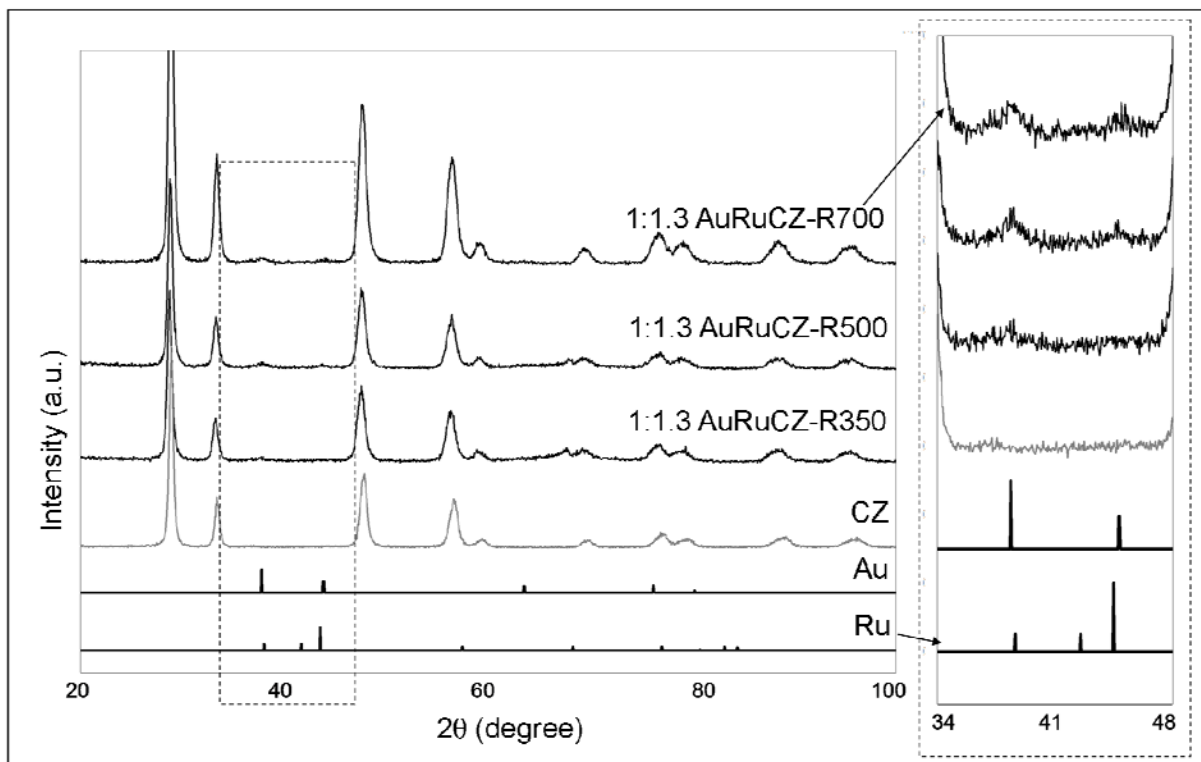


**Figure 2.** X-ray diffraction patterns of 1:0.1.3 AuRuCZ reduced at increasing temperatures. The insets show enlarged diagrams.

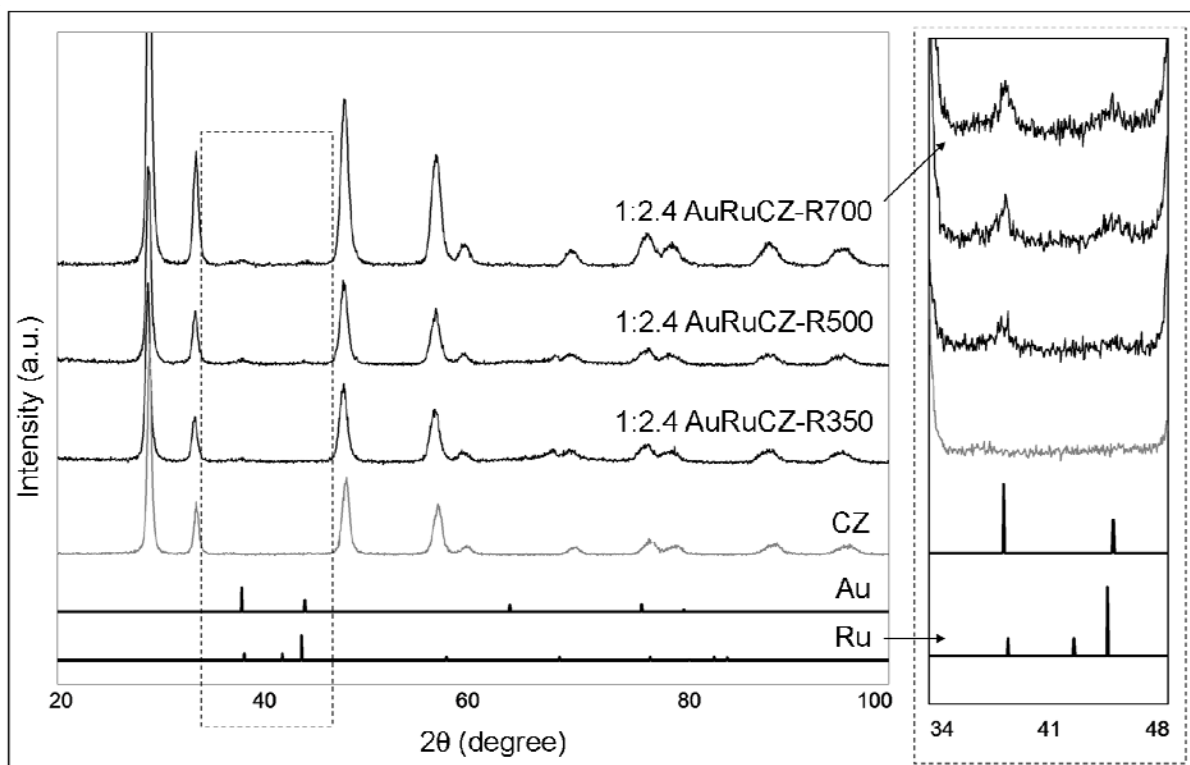


**Figure 3.** X-ray diffraction patterns of 1:2.4 AuRuCZ reduced at increasing temperatures. The insets show enlarged diagrams.

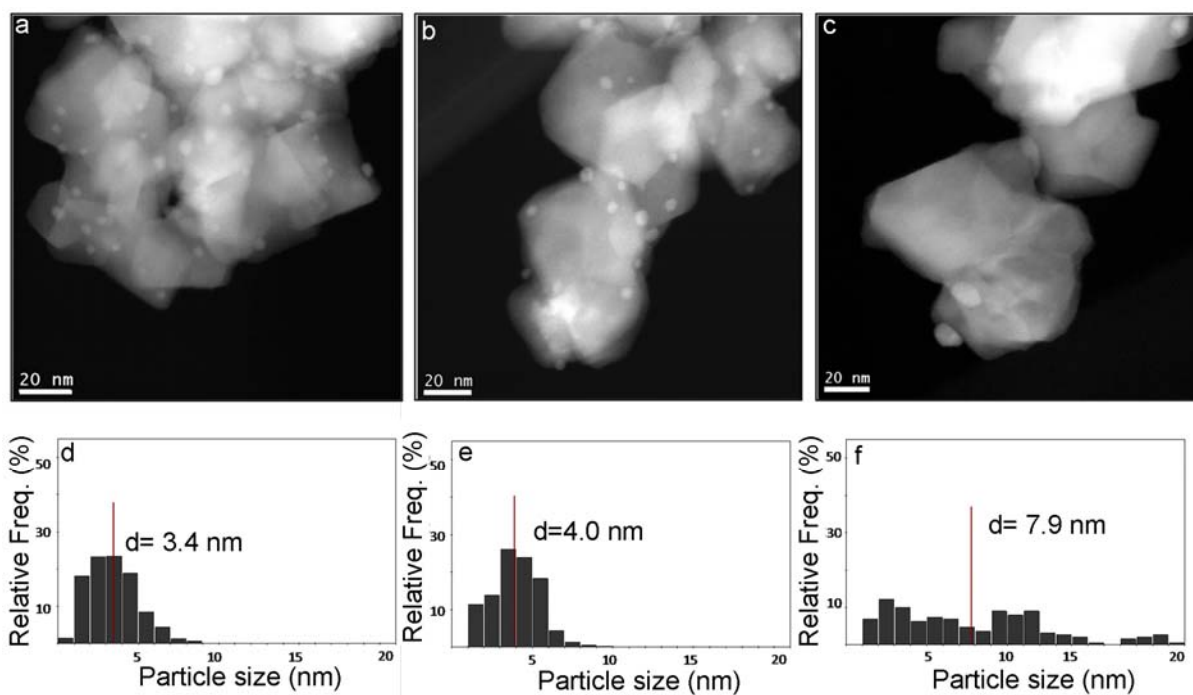


**Figure 4:** Representative HAADF-STEM images and particle size distribution (PSD) corresponding to 1:0.7AuRuCZ catalyst reduced at 350 °C a) and d), 500 °C b) and e) and 700 °C c) and f).

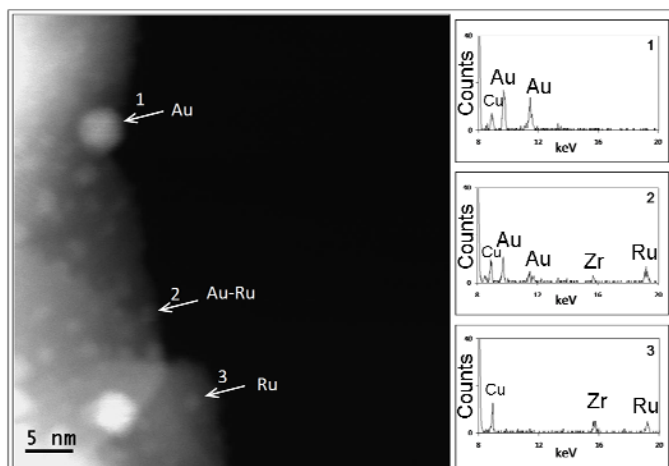


**Figure 5** STEM-XEDS of individual particles showing monometallic and bimetallic nanoparticles in 1:0.7AuRuCZ-R350. Each spectrum is labeled with a number. This number is the one shown close to the arrow pointing to each nanoparticle.

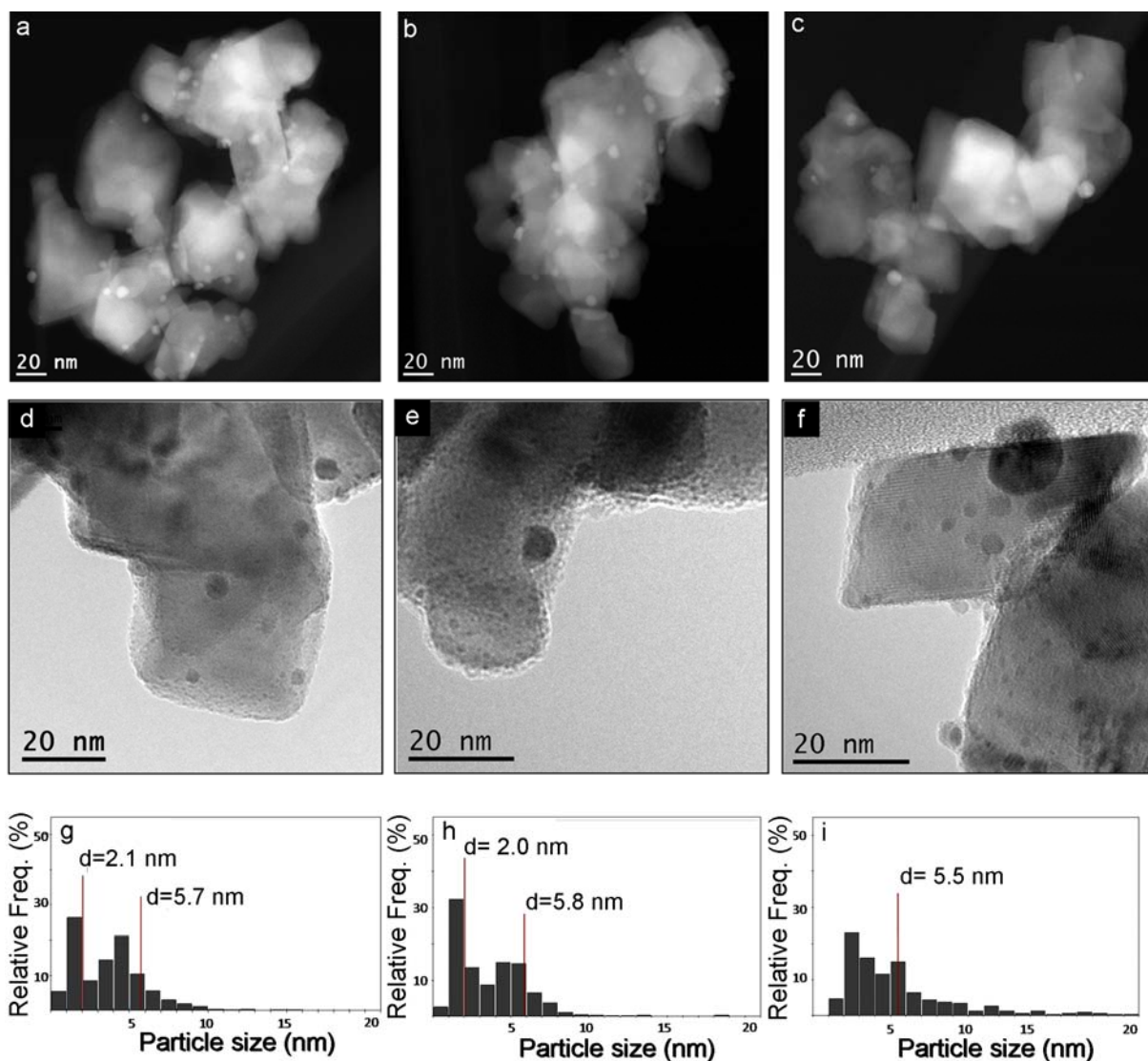


**Figure 6:** Representative HAADF-STEM, HREM images and particle size distribution (PSD) corresponding to 1:1.3 AuRuCZ catalyst reduced at 350 °C a), d) g), 500 °C b), e) h) and 700 °C c), f) i).

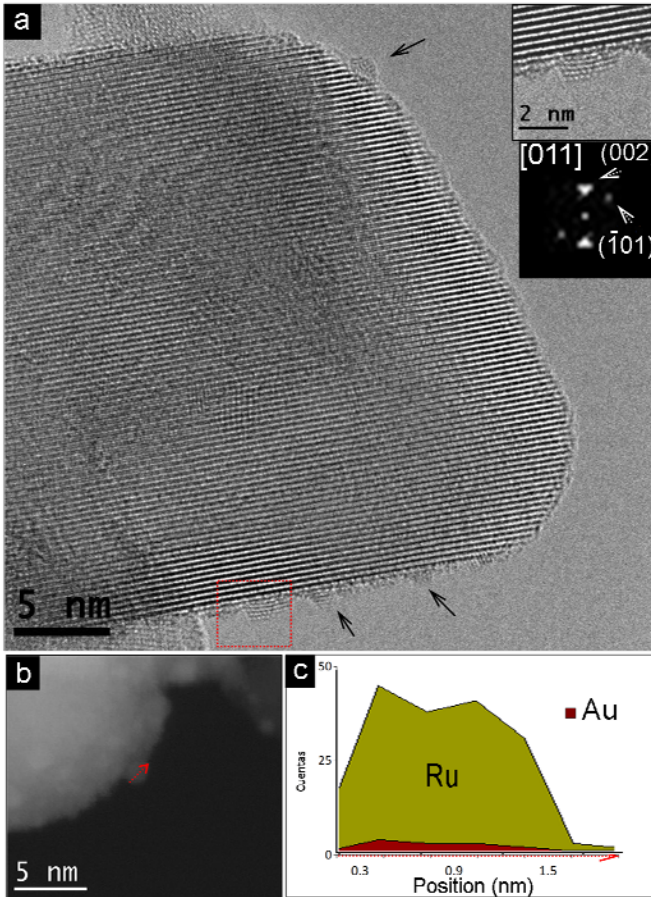


**Figure 7:** a) Representative HREM image of 1:1.3AuRuCZ sample showing small Ruthenium nanoparticles as evidenced by the analysis of the DDP shown as an inset. b) HAADF-STEM image of an area showing small ruthenium nanoparticles as the one marked with an arrow and analyzed in c).

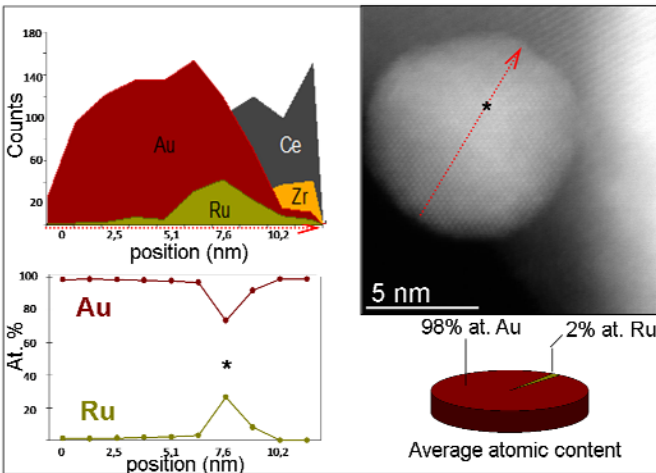


**Figure 8:** XEDS analysis along the marked path in the HAADF-STEM image of a nanoparticle in 1:1.3AuRuCZ.

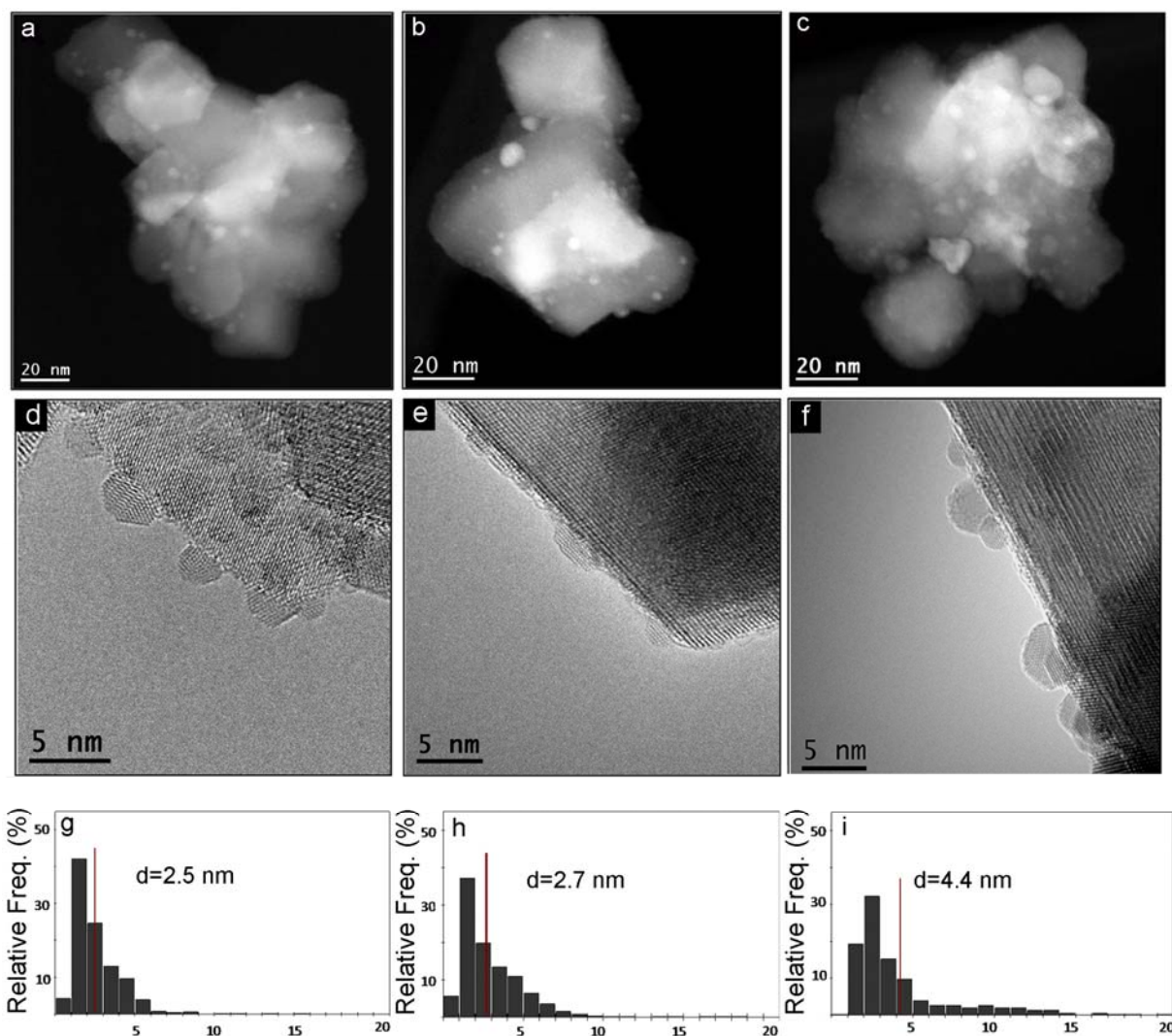


**Figure 9:** Representative HAADF-STEM, HREM images and particle size distribution (PSD) corresponding to 1:2.4 AuRuCZ catalyst reduced at 350 °C a), d) g) , 500 °C b), e) h) and 700 °C c), f) i).

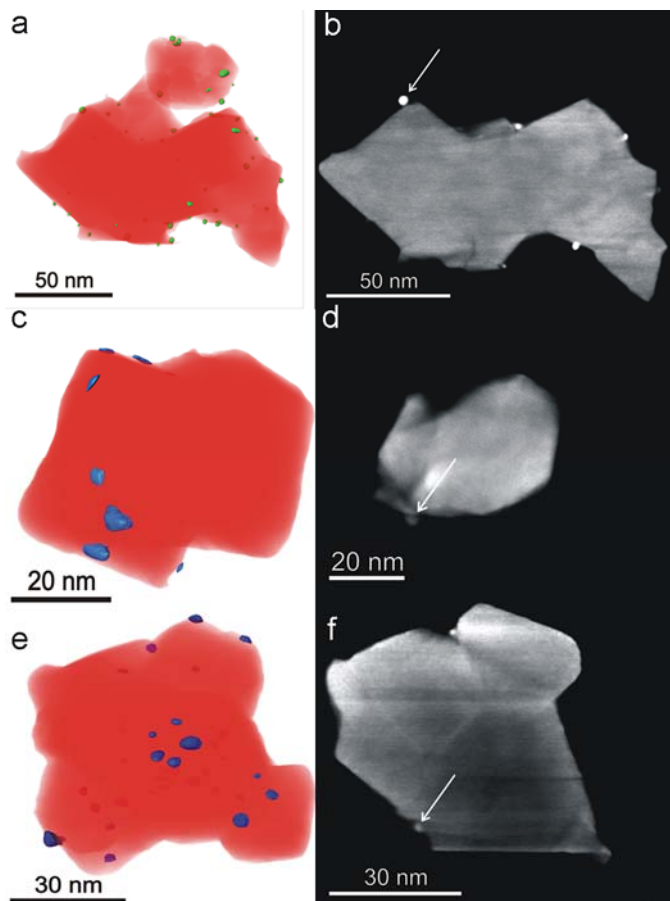


**Figure 10** Visualizations of the 3-D reconstruction of the samples (a) AuCZ, (c) RuCZ and (e) 1:2.4 AuRuCZ. Slices (orthoslice) through the 3-D reconstructions are presented from (b) AuCZ, (d) RuCZ and (f) 1:2.4 AuRuCZ, respectively. Metal particles located on the surface are marked with arrows.

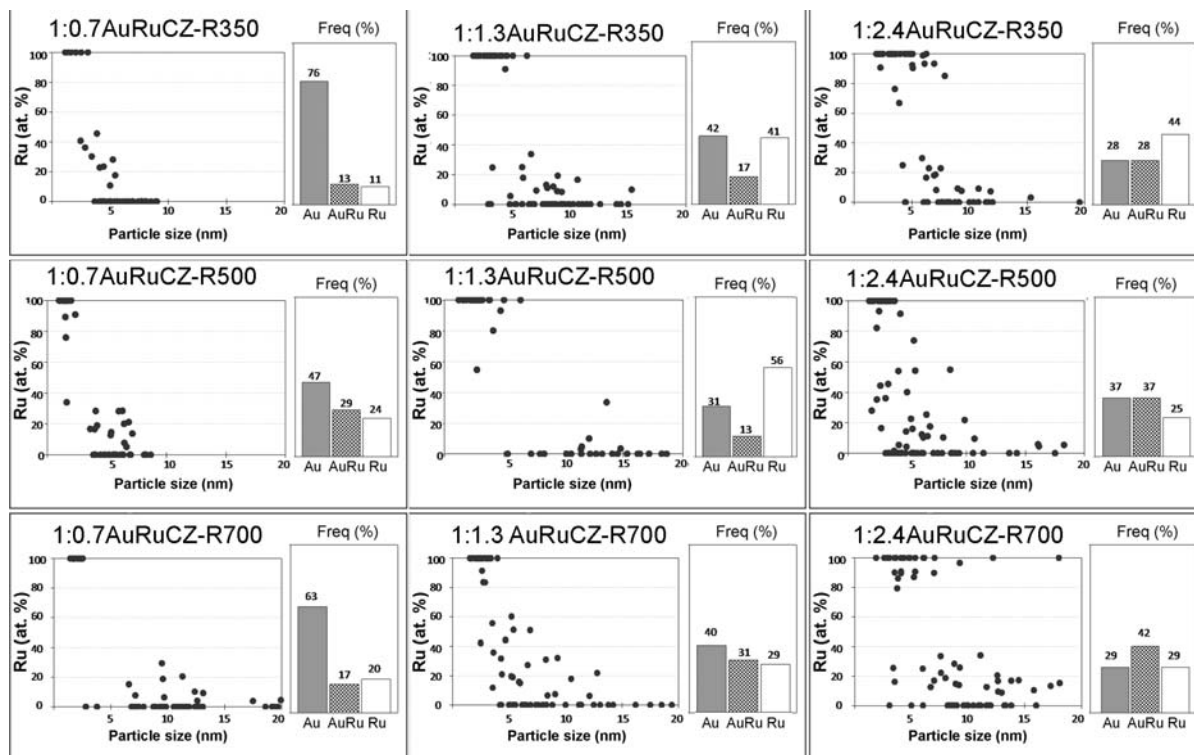


**Figure 11:** Composition (Ru at. %) versus size and percentage of particle types (Au, Ru or AuRu) for every catalysts reduced at 350, 500 and 700 °C.

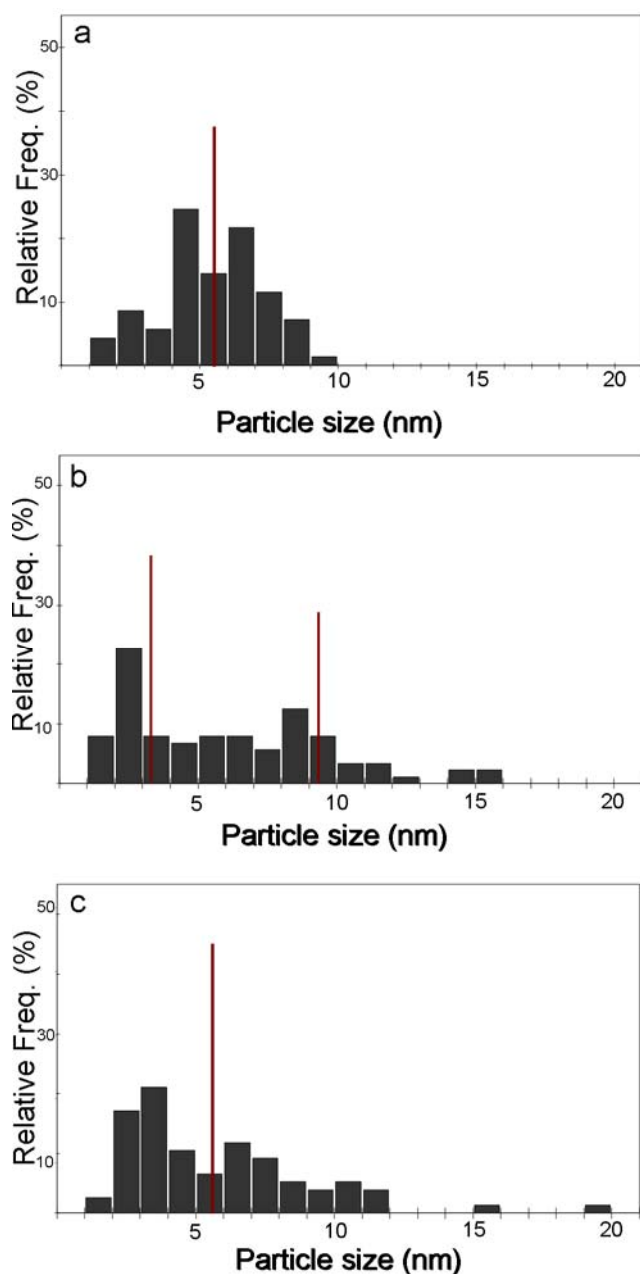


**Figure 12:** Particle size distribution calculated from the nanoanalytical studies of the three catalysts reduced at 350 °C a) 1:0.7 AuRuCZ b) 1:1.3 AuRuCZ and c) 1:2.4 AuRuCZ.

**Table 1.** Values of Au and Ru content

Catalyst	Weight (%) <sup>a)</sup>		Atomic ratio Au:Ru	Atomic content (%) <sup>b)</sup>	
	Au	Ru		Au	Ru
AuCZ	1.00 ± 0.02			100	
RuCZ		0.97 ± 0.10			100
1:0.7 AuRuCZ	0.99 ± 0.02	0.33 ± 0.02	1:0.7	61	39
1:1.3 AuRuCZ	0.98 ± 0.02	0.68 ± 0.08	1:1.3	43	57
1:2.4 AuRuCZ	0.98 ± 0.02	1.21 ± 0.02	1:2.4	29	71

a) Data obtained from ICP-AES analysis. b) Data calculated from atomic ratios. Au atomic content % =  $(N_{Au}) \times 100 / (N_{Au} + N_{Ru})$  and Ru atomic content % =  $100 - \text{Au atomic content \%}$ .

**Table 2.** Binding energies values of gold and ruthenium phases on the mono- and bimetallic catalysts as determined by XPS measurements.

Catalyst	Peak designation			Relative % of Ru species	
	Au 4f <sub>7/2</sub> <sup>a</sup>	Ru 3d <sub>5/2</sub> <sup>b</sup>		Ru 3d <sub>5/2</sub> <sup>b</sup>	
	BE	Low BE	High BE	Low BE	High BE
AuCZ	84.3	-	-	-	-
1:0.7AuRuCZ-R350	84.3	281.9	283.0	89.3	10.7
1:1.3AuRuCZ-R350	84.3	281.6	282.7	73.8	26.2
1:1.3AuRuCZ-R500	84.3	281.7	282.9	78.3	21.7
1:1.3AuRuCZ-R700	84.3	281.3	282.8	77.4	22.6
1:2.4AuRuCZ-R350	84.3	281.8	283.1	79.1	20.9
1:2.4AuRuCZ-R500	84.3	281.8	283.0	78.1	21.9
1:2.4AuRuCZ-R700	84.3	281.6	282.9	81.8	18.2
RuCZ	-	281.6	282.7	72.1	27.9

<sup>a</sup> The XPS Au 4f<sub>7/2</sub> binding energy is consistent with zero-valent Au

<sup>b</sup> Peaks designated as Low BE are assigned to RuO<sub>2</sub> and those referred as High BE could correspond to RuO<sub>3</sub> or very small RuO<sub>2</sub> nanoparticles.

**Table 3.** Surface elemental composition of AuRuCZ catalyst as determined by XPS.

Catalyst	Surface concentration (atomic %)					Surface atomic fraction Ru
	Ce	Zr	O	Au	Ru	
1:0.7AuRuCZ-R350	25.3	12.9	58.2	0.8	2.8	78
1:1.3AuRuCZ-R350	25.5	13.1	57.8	0.3	3.2	91
1:1.3AuRuCZ -R500	23.6	11.8	62.3	0.4	2.0	83
1:1.3AuRuCZ -R700	26.3	12.8	57.9	0.3	2.7	90
1:2.4AuRuCZ-R350	28.4	11.4	55.7	0.3	4.3	93
1:2.4AuRuCZ -R500	28.9	11.6	55.2	0.3	4.1	93
1:2.4AuRuCZ -R700	29.5	11.6	55.3	0.3	3.3	92

**Table 4.** Particle size and dispersion estimated from the PSDs of the two monometallic catalysts

Catalyst	d(nm)	D (%)	Catalyst	d(nm)	D(%)
AuCZ-R350	2.4 ± 0.1	41	RuCZ-R350	1.5± 0.1	49
AuCZ-R500	3.8 ± 0.2	17	RuCZ-R500	1.7± 0.1	47
AuCZ-R700	11.5 ± 0.5	11	RuCZ-R700	2.2± 0.1	38

**Table 5:** Particle size estimated from PSDs and XRD of the three bimetallic catalyst. Dispersion estimated from PSDs

Catalyst	Particle size (nm)				D (%)
	d <sup>a)</sup>	d <sub>ps</sub>	d <sub>pV</sub>	d <sub>XRD</sub>	
1:0.7 AuRuCZ-R350	3.4±0.1	4.7	5.3	- <sup>b)</sup>	28
1:0.7 AuRuCZ-R500	4.0±0.1	4.7	5.3	- <sup>b)</sup>	27
1:0.7 AuRuCZ-R700	7.9±0.4	13.2	14.9	16.2	11
1:1.3 AuRuCZ-R350	3.6±0.1	6.6	8.1	8.4	23
1:1.3 AuRuCZ-R500	3.7±0.1	6.8	9.1	10.9	22
1:1.3 AuRuCZ-R700	5.5±0.2	10.9	13.5	14.2	13
1:2.4 AuRuCZ-R350	2.5±0.1	5.6	7.8	14.2	26
1:2.4 AuRuCZ-R500	2.9±0.1	6.4	9.1	14.6	23
1:2.4 AuRuCZR700	4.4±0.2	11.7	15.7	19.1	14

a) Mean Particle size considering unimodal distribution

b) Not estimated

**Table 6:** Size range of each type of particle, average size and the average Au content in the case of the bimetallics

Catalyst	Ru		Au		AuRu		Au(%)
	Range (nm)	d (nm)	Range (nm)	d(nm)	Range (nm)	d(nm)	
1:0.7 AuRuCZ -R350	1.1 -3.1	2	3.7 -9.0	6.2	2.4 - 5.4	4.1	73
1:0.7 AuRuCZ -R500	1.0 -2.0	1.5	3.9 -8.8	5.9	1.5 - 7.2	4.7	82
1:0.7 AuRuCZ -R700	1.4 - 2.5	2	2.8 -20.0	11.3	6.6 -20.0	11.6	92
1:1.3 AuRuCZ -R350	1.6 - 6.3	2.8	2.9 - 15.0	8.6	3.3 - 15.3	7.7	86
1:1.3 AuRuCZ -R500	1.2 - 6.4	2.7	5.3 -18.6	12.5	2.7 - 14.8	9.3	86
1:1.3 AuRuCZ -R700	1.5 - 4.0	2.6	4.2 -19.4	9.3	2.5 - 12.8	6.1	79
1:2.4 AuRuCZ -R350	1.9 - 6.3	3.3	4.4 - 19.6	8.9	2.2 - 15.3	7	78
1:2.4 AuRuCZ -R500	1.8 - 3.9	2.9	3.2 - 17.5	7.2	2.0 - 18.3	6.3	88

1:2.4 AuRuCZ -R700	1.9 - 18.0	5.1	3.1 - 16.0	10.2	3.4 - 23.0	10	66
--------------------	------------	-----	------------	------	------------	----	----

**Table 7:** values of Ru molar contents for the three AuRuCZ-R350 catalysts determined by XEDS, ICP and XPS.

Catalyst	Ru(%)XEDS	Ru(%) ICP	Ru(%) XPS
1:0.7AuRuCZ-R350	4	39	72
1:1.3AuRuCZ-R350	7	56	91
1:2.4AuRuCZ-R350	20	71	92

**Table 8:** Intrinsic catalytic activities per exposed metal atom as a function of the ruthenium content of the catalysts reduced at 350 °C.

Catalyst	Conversion (%) <sup>a)</sup>	Selectivity (%) <sup>b)</sup>	TOF (h <sup>-1</sup> )
RuCZ-R350	29	> 99	31
AuCZ-R350	10	> 99	32
1:0.7AuRuCZ-R350	27	> 99	49
1:1.3AuRuCZ-R350	33	> 99	100
1:2.4AuRuCZ-R350	31	> 99	109

a) Conversion after 3 hours of reaction.

b) Selectivity towards 1-octanal

## Table of content.

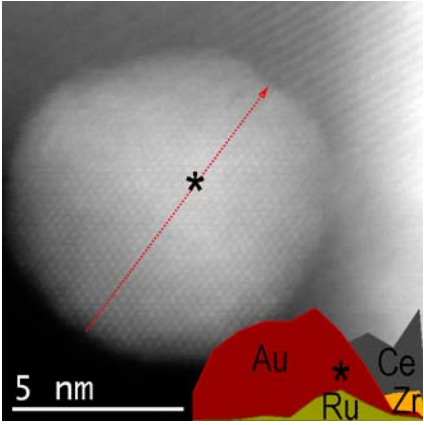
**A series of supported gold–ruthenium bimetallic catalysts of varying Au:Ru molar ratios are prepared onto ceria–zirconium mixed oxide (Ce<sub>0.62</sub>Zr<sub>0.38</sub>O<sub>2</sub>).** A combination of macroscopic and nanometric scale techniques based on Scanning Transmission Electron Microscopy (STEM) are used to characterize their structural and chemical features and the resistance against sintering. Catalytic behaviour is tested in the selective oxidation of octanol.

## Keyword

Supported bimetallic catalysts, STEM-XEDS, Gold, Ruthenium, Octanol oxidation.

Lidia E. Chinchilla, Carol Olmos, Mert Kurttepli, Sara Bals, Gustaaf Van Tendeloo, Alberto Villa, Laura Prati, Ginesa Blanco, José J. Calvino, Xiaowei Chen, Ana B. Hungría\*

## Combined Macroscopic, Nanoscopic and Atomic-scale Characterization of Gold-Ruthenium Bimetallic Catalysts for Octanol Oxidation



- 
- <sup>1</sup> G. C. Bond, P. A. Sermon, G. Webb, D. A. Buchanan, P. B. Wells, *J. Chem. Soc. Chem. Commun.* **1973**, 444.
- <sup>2</sup> G. J. Hutchings, *J. Catal.* **1985**, 96, 292.
- <sup>3</sup> M. Haruta, T. Kobayashi, H. Sano, N. Yamada, *Chem. Lett.* **1987**, 2, 405.
- <sup>4</sup> G.C. Bond, D.T. Thompson, *Catal. Rev. -Sci. Eng.* **1999**, 41, 319.
- <sup>5</sup> L. Prati, M. Rossi, *J. Catal.* **1998**, 176, 552.
- <sup>6</sup> A.S. K. Hashmi, G. J. Hutchings, *Angew. Chem. Int. Ed.* **2006**, 45, 7896.
- <sup>7</sup> M. Haruta, *Cat. Today.* **1997**, 36, 153.
- <sup>8</sup> M. Haruta, *Chem. Rec.* **2003**, 3, 75.
- <sup>9</sup> A. Abad, C. Almela, A. Corma, H. Garcia, *Tetrahedron.* **2008**, 62, 6666.
- <sup>10</sup> J. K. Edwards, B. E. Solsona, P. Landon, A. F. Carley, A. Herzing, C. J. Kiely, G. J. Hutchings, *J. Catal.* **2005**, 236, 69.
- <sup>11</sup> W. Hou, N. A. Dehm, R. W. J. Scott, *J. Catal.* **2008**, 253, 22.
- <sup>12</sup> G. J. Hutchings, C. J. Kiely, *Accounts Chem. Res.* **2013**, 46, 1759.
- <sup>13</sup> S. Marx, A. Baiker, *J. Phys. Chem. C.* **2009**, 113, 6191.
- <sup>14</sup> N. Dimitratos, A. Villa, D. Wang, F. Porta, D. Su, L. Prati, *J. Catal.* **2006**, 244, 113.
- <sup>15</sup> L. E. Chinchilla, C. M. Olmos, A. Villa, A. Carlsson, L. Prati, X. Chen, G. Blanco, J. J. Calvino, A. B. Hungria, *Catal. Today.* **2015**, 253, 178.
- <sup>16</sup> L. Prati, F. Porta, Di Wang, A. Villa, *Catal. Sci. Technol.*, **2011**, 1, 1624.
- <sup>17</sup> A. Villa, C. E. Chan-Thaw, S. Campisi, C. L. Bianchi, D. Wang, P. G. Kotula, C. Kubel and L. Prati, *Phys.Chem.Chem.Phys.*, **2015**, 17, 28171
- <sup>18</sup> L. Guczi, A. Beck, A. Horváth, Zs. Koppány, G. Stefler, K. Frey, I. Sajó, O. Geszti, D. Bazin, J. Lynch, *J. Mol. Catal. A: Chem.* **2003**, 204–205, 545.

- 
- <sup>19</sup> H. Yang, W. Vogel, C. Lamy, and N. Alonso-Vante, *J. Phys. Chem. B* **2004**, 108, 11024.
- <sup>20</sup> P. Lu, T. Teranishi, K. Asakura, M. Miyake, N. Toshima, *J. Phys. Chem. B* **1999**, 103, 9673.
- <sup>21</sup> A.A. Herzing, M. Watanabe, J. K. Edwards, M. Conte, Z.R Tang, G. J. Hutchings and C. J. Kiely, *Faraday Discuss.*, **2008**, 138, 337.
- <sup>22</sup> W. Diao, J. Meynard, M. Tengco, J. R. Regalbuto, J.R. Monnier, *ACS Catal.* **2015**, 5, 5123.
- <sup>23</sup> M. Conte, A. F. Carley, G. Attard, A. A. Herzing, C. J. Kiely, G. J. Hutchings, *J. Catal.* **2008**, 257, 190.
- <sup>24</sup> R.E Lakis, C.E. Lyman, H.G. Stenger, *J. Catal.* **1995**, 154, 261.
- <sup>25</sup> L. Bednarova, C. E. Lyman, E. Rytter, and A. Holmen *J. Catal.* **2002**, 211, 335.
- <sup>26</sup> L. Prati, A. Villa, C. Campione, P. Spontoni, *Top. Catal.* **2007**, 44, 319.
- <sup>27</sup> W. Zou, R.D. González, *Catal. Today* **1992**, 15, 443.
- <sup>28</sup> S.E. Collins, J.M. Cies, E. del Rio, M.Lopez-Haro, S.Trasobares, J.J. Calvino, J.M. Pintado, S.Bernal, *J. Phys. Chem. C* **2007**, 111, 14371.
- <sup>29</sup> M. P. Yeste, J. C. Hernández, S. Bernal, G. Blanco, J. J. Calvino, J. A. Pérez-Omil, J. M. Pintado, *Chem. Mater.* **2006**, 18, 2750.
- <sup>30</sup> M. P. Yeste, J. C. Hernández, S. Trasobares, S. Bernal, G. Blanco, J. J. Calvino, J. A. Pérez-Omil, J. M. Pintado, *Chem. Mater.* **2008**, 20, 5107.
- <sup>31</sup> L.F. Liotta, G. Di Carlo, A. Longo, G. Pantaleo, A.M. Venezia, *Catal. Today.* **2008**, 139, 174.
- <sup>32</sup> J. M. Cies, E. del Río, M. López-Haro, J. J. Delgado, G. Blanco, S. Collins, J. J. Calvino, S. Bernal, *Angew. Chem. Int. Ed.* **2010**, 49, 9744.
- <sup>33</sup> Y. Kitsudo, A. Iwamoto, H. Matsumoto, K. Mitsuhashi, T. Nishimura, M. Takizawa, T. Akita, Y. Maeda, Y. Kido, *Surf. Sci.* **2009**, 603, 2108.

- 
- <sup>34</sup> C. Elmasides, D. I. Kondarides, W. Gruhnert, and X. E. Verykios, *J. Phys. Chem. B.* **1999**, 103, 5227.
- <sup>35</sup> J.C.H. Spence, *Experimental High-Resolution Electron Microscopy*, Oxford University Pr. **1998**.
- <sup>36</sup> M. Lopez-Haro, J. A. Perez-Omil, J. C. Hernandez-Garrido, S. Trasobares, A. B. Hungria, J. M. Cies, P. A. Midgley, P. Bayle-Guillemaud, A. Martinez-Arias, S. Bernal, J. J. Delgado, J. J. Calvino, *Chem.Cat.Chem.* **2011**, 3, 1015.
- <sup>37</sup> S. Bernal, J.J. Calvino, J.M. Gatica, C.L. Cartes, J.M. Pintado, *Catalysis by Ceria and Related Materials*, A. Trovarelli, Ed. Imperial College Press: London, **2002**.
- <sup>38</sup> S. Bernal, R.T. Baker, A. Burrows, J. J. Calvino, C. J. Kiely, C. Lopez-Cartes, J. A. Perez-Omil, J.M. Rodriguez-Izquierdo *Surf. Interface Anal.* **2000** 29, 411.
- <sup>39</sup> S. Bernal, F.J. Botana, J.J. Calvino, C. Lopez-Cartes, J.A. Perez-Omil, J.M. Rodriguez-Izquierdo, *Ultramicroscopy* **1998**, 72, 135.
- <sup>40</sup> S. Bernal , F.J. Botana, J.J. Calvino, G.A. Cifredo, J.A. Perez-Omil, J.M. Pintado, *Catal. Today* **1995**, 23, 219.
- <sup>41</sup> M. Lopez-Haro, J. J. Delgado, J. C. Hernández-Garrido, J. D. D. López-Castro, C. Mira, S.Trasobares, A. B. Hungría., J. A. Pérez-Omil, J. J. Calvino. *Electron Microscopy of Nanoparticles. Handbook of Nanoscopy.* **2012**.
- <sup>42</sup> R.T. Baker, J. J. Calvino, C. Lopez-Cartes, C. Mira, J. A. Perez-Omil, J.M. Rodriguez-Izquierdo. *Electron Micros. Analysis*, **1999**, 161, 537.
- <sup>43</sup> P.D. Nellist, S.J. Penycook, *Ultramicroscopy* **1999**, 78, 111.
- <sup>44</sup> E.M. James, N.D: Browning, *Ultramicroscopy* **1999**, 78, 125.
- <sup>45</sup> H. Okamoto, T.B. Massalski. *Bulletin of Alloy Phase Diagrams*, **1984**, 5, 388.
- <sup>46</sup> R. Zanella, S. Giorgio, C. Henry, C. Louis, *J. Phys. Chem. B.* **2002**, 106, 7634.